

See discussions, stats, and author profiles for this publication at: <https://www.researchgate.net/publication/263543254>

# Synthesis, Characterization, and Electrochemistry of Nanotubular Polypyrrole and Polypyrrole-Derived Carbon Nanotubes

ARTICLE in THE JOURNAL OF PHYSICAL CHEMISTRY C · JUNE 2014

Impact Factor: 4.77 · DOI: 10.1021/jp502862d

---

CITATIONS

10

READS

111

## 11 AUTHORS, INCLUDING:



Gordana Cirić-Marjanović

University of Belgrade

80 PUBLICATIONS 1,860 CITATIONS

[SEE PROFILE](#)



Igor Pasti

University of Belgrade

69 PUBLICATIONS 529 CITATIONS

[SEE PROFILE](#)



Jadranka Trervas-Sejdic

University of Auckland

199 PUBLICATIONS 3,489 CITATIONS

[SEE PROFILE](#)



Miroslava Trchová

Academy of Sciences of the Czech Republic

174 PUBLICATIONS 5,773 CITATIONS

[SEE PROFILE](#)

# Synthesis, Characterization, and Electrochemistry of Nanotubular Polypyrrole and Polypyrrole-Derived Carbon Nanotubes

Gordana Ćirić-Marjanović,<sup>\*,†</sup> Slavko Mentus,<sup>†</sup> Igor Pašti,<sup>†</sup> Nemanja Gavrilov,<sup>†</sup> Jugoslav Krstić,<sup>‡</sup> Jadranka Travas-Sejdic,<sup>§,||</sup> Lisa T. Strover,<sup>§,||</sup> Jitka Kopecká,<sup>⊥</sup> Zuzana Moráková,<sup>#</sup> Miroslava Trchová,<sup>#</sup> and Jaroslav Stejskal<sup>#</sup>

<sup>†</sup>Faculty of Physical Chemistry, University of Belgrade, Studentski trg 12-16, 11158 Belgrade, Serbia

<sup>‡</sup>Institute of Chemistry, Technology and Metallurgy, Department of Catalysis and Chemical Engineering, University of Belgrade, Njegoševa 12, 11000 Belgrade, Serbia

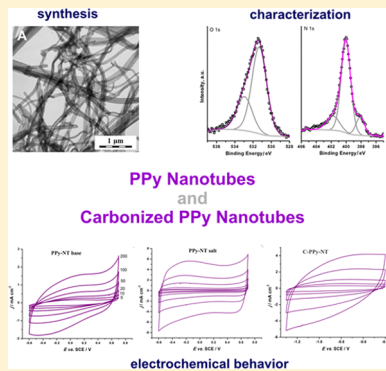
<sup>§</sup>Polymer Electronics Research Centre, School of Chemical Sciences, University of Auckland, 23 Symonds Street, Auckland, New Zealand

<sup>||</sup>MacDiarmid Institute for Advanced Materials and Nanotechnology, Victoria University of Wellington, P.O. Box 600, Wellington 6140, New Zealand

<sup>⊥</sup>Faculty of Chemical Engineering, Institute of Chemical Technology Prague, 166 28 Prague 6, Czech Republic

<sup>#</sup>Institute of Macromolecular Chemistry, Academy of Sciences of the Czech Republic, 162 06 Prague 6, Czech Republic

**ABSTRACT:** Polypyrrole nanotubes (PPy-NTs) were prepared by the oxidation of pyrrole with iron(III) chloride in the presence of a structure-guiding agent, methyl orange. Upon carbonization of the salt form of PPy-NTs, the conducting nitrogen-containing nanotubular carbonaceous material (C-PPy-NT) was obtained. The morphology, structure, and physicochemical properties of PPy-NTs in salt and base form as well as C-PPy-NTs were investigated by transmission electron microscopy, Fourier transform infrared and Raman spectroscopies, conductivity measurements, elemental microanalysis, inductively coupled plasma optical emission spectroscopy, X-ray photoelectron spectroscopy, and nitrogen physisorption. Results of the material characterization were linked to their electrochemical behavior. Specific capacitance of around  $120 \text{ F g}^{-1}$  at low potential sweep rate of  $5 \text{ mV s}^{-1}$  was observed for original PPy-NTs. However, when the potential sweep rate was increased to  $100 \text{ mV s}^{-1}$ , PPy-NT salt retained the value of specific capacitance, while the capacitance of PPy-NT base decreased by 70%. Upon carbonization of PPy-NT salt, the specific capacitance was doubled and capacitance fade measured in the interval  $5\text{--}100 \text{ mV s}^{-1}$  was determined to be around 45%. It is proposed that the absolute value of specific capacitance is determined by specific surface area and surface functional groups, while the capacitance fade is determined by the conductivity of the electrode material. In this manner, a linear relationship between the percent of capacitance fade and the logarithm of the conductivity was revealed. C-PPy-NTs were also tested as an electrocatalyst for the oxygen reduction reaction (ORR) in alkaline media. High ORR activity was observed, characterized by the onset potential of  $-0.1 \text{ V}$  versus saturated calomel electrode and the apparent number of electrons consumed per oxygen molecule higher than 3. Appreciable ORR activity can be linked with a high fraction of mesopores and the presence of surface functional groups, especially pyridinic and pyrrolic nitrogens, and also with a high degree of structural disorder.



## INTRODUCTION

A large number of various carbon nanostructures have been reported during the past three decades, e.g., fullerene,<sup>1</sup> carbon nanotubes (CNTs),<sup>2</sup> nanospheres,<sup>3</sup> nanofibers,<sup>4</sup> nanohorns,<sup>5</sup> and graphene.<sup>6</sup> It has been revealed that heteroatom doping, i.e., the intentional introduction of other atoms into the structure of the carbon nanomaterials, can significantly affect their structure and properties.<sup>7–10</sup> The nitrogen-containing carbon nanostructures (NCNSs), especially one-dimensional (1-D) NCNSs such as nitrogen-containing CNTs (NCNTs),<sup>11–13</sup> have received much more attention than any other heteroatom-containing carbon nanomaterials because 1-D NCNSs have shown highly versatile applicability. It has been

demonstrated that NCNTs could be successfully used in energy conversion and storage (fabrication of batteries<sup>14</sup> and electrochemical capacitors,<sup>15</sup> preparation of electrocatalysts for low-temperature fuel cell applications,<sup>16</sup> hydrogen storage,<sup>17</sup> etc.), sensor technology (chemiresistors,<sup>18</sup> electrochemical sensors/biosensors<sup>19</sup>), catalysis,<sup>20</sup> environmental protection (preparation of adsorbents<sup>21</sup>), (nano)electronics,<sup>22</sup> biology and medicine (immobilization of biomolecules,<sup>23</sup> fabrication of drug delivery systems,<sup>24</sup> therapeutic management of athero-

Received: March 22, 2014

Revised: May 19, 2014

Published: June 12, 2014

sclerotic disease,<sup>25</sup> etc.), polymer reinforcement,<sup>26</sup> and preparation of electrorheological fluids.<sup>27</sup>

Synthesis of NCNTs has been successfully accomplished by various chemical reactions (reaction of carbon halides with sodium azide,<sup>28</sup> reduction of pentachloropyridine with metallic sodium<sup>29</sup>), arc-discharge of carbon electrodes in a nitrogen-containing gas atmosphere,<sup>30</sup> laser ablation,<sup>31</sup> magnetron sputtering of a graphite in a nitrogen atmosphere,<sup>32</sup> graphite resistive heating under high nitrogen pressure,<sup>33</sup> exposure of graphite to nitrogen plasma,<sup>34</sup> pyrolysis of nitrogen-containing aliphatic<sup>35</sup> and carbocyclic aromatic compounds,<sup>36</sup> pyrolysis of nitrogen-containing heterocyclic aromatic compounds,<sup>37</sup> pyrolysis of hydrocarbons<sup>38</sup> and oxygen-containing organic compounds<sup>39</sup> in nitrogen-containing gas phase, functionalization of CNTs surfaces by functional groups (treatment of CNTs with nitrogen-containing gas plasma<sup>40</sup> or nitrogen ions,<sup>41</sup> treatment of CNTs and/or oxidized/oxygen-functionalized CNTs with nitrogen-containing inorganic<sup>42</sup> or organic compounds<sup>43</sup>), the pyrolysis of nitrogen-containing ion-exchange resin,<sup>44</sup> and carbonization of nitrogen-containing polymer nanotubes.<sup>45</sup> Carbonization of conducting polymers with nanotubular morphology has emerged in recent years as an efficient way to prepare NCNTs.<sup>46,47</sup> Polyaniline nanotubes and nanorods<sup>15,16,48–52</sup> and polypyrrole nanotubes (PPy-NTs)<sup>45,53–61</sup> are the most frequently used nitrogen-containing conducting polymer precursors in the synthesis of NCNTs.

In the present work, NCNTs were prepared by the carbonization of PPy-NTs, which were synthesized by using a structure-guiding agent, methyl orange.<sup>62–64</sup> Structure and properties of C-PPy-NTs as well as the starting PPy-NTs in their salt and base forms were investigated by various techniques. Synthesized C-PPy-NTs have been tested as electrode materials for supercapacitors and electrocatalysts for oxygen reduction reaction (ORR). Electrochemical properties of the prepared materials were connected to their physicochemical properties.

## MATERIALS AND METHODS

**Synthesis of PPy-NTs.** PPy-NTs were prepared as follows:<sup>63,64</sup> 82 mg (0.25 mmol) of methyl orange was dissolved in 60 mL of water at 5 °C and 0.36 mL (5 mmol) of pyrrole. A precooled solution of 1.35 g (5 mmol) of iron(III) chloride hexahydrate in 20 mL was added dropwise, and the total volume was adjusted to 100 mL with water. All reactants were supplied by Aldrich. Thus, the concentrations of reactants were 0.05 M pyrrole, 0.05 M iron(III) chloride, and 2.5 mM methyl orange (MO), sodium 4-[4-(dimethylamino)phenylazo]benzenesulfonate. The mixture was thermostated to 5 °C and gently stirred for 24 h. The solids were separated and purified by Soxhlet extraction with acetone to remove residual reactants, then rinsed with ethanol and dried at 40 °C in vacuo. A part of polypyrrole hydrochloride was converted to a polypyrrole base by the overnight immersion in 1 M ammonium hydroxide. For spectroscopic analysis, 4-[4-(dimethylamino)-phenylazo]benzenesulfonic acid (MO-A) was prepared from MO by ion-exchange technique using hydriodic acid.

**Carbonization.** PPy-NTs (in salt form) were placed in an electric oven in a stream of nitrogen. The heating was switched on, and the temperature increased at a rate of 20 °C min<sup>-1</sup> to 650 °C. After the target temperature was reached, the heating was switched off, and produced C-PPy-NTs were left to cool to room temperature.

**Characterization.** Transmission electron microscopy (TEM) micrographs were taken with a Tecnai Spirit G2 microscope (FEI, Brno, Czech Republic).

Fourier-transform infrared (FTIR) spectra of the powders dispersed in potassium bromide pellets have been recorded with a Thermo Nicolet NEXUS 870 FTIR Spectrometer with a DTGS TEC detector in the 400–4000 cm<sup>-1</sup> wavenumber region.

Raman spectra of the powders were measured with a Renishaw InVia Reflex Raman microspectrometer. The spectra were excited with an Ar-ion 514 nm, HeNe 633 nm, or a diode 785 nm lasers. A research-grade Leica DM LM microscope with an objective magnification 50× was used to focus the laser beam on the sample placed on an X-Y motorized sample stage. The scattered light was analyzed by the spectrograph with holographic gratings 2400, 1800, and 1200 lines mm<sup>-1</sup> for Ar-ion 514 nm, HeNe 633 nm, and diode 785 nm lasers, respectively. A Peltier-cooled CCD detector (576 × 384 pixels) registered the dispersed light.

Conductivity measurements were performed by compressing the powders between stainless steel pistons in an insulating plastic tube at room temperature with an ac bridge (Wayne Kerr Universal Bridge B 224) operating at a fixed frequency of 1.0 kHz (two-probe method). The pressure was maintained at 125 MPa or ~500 MPa at the sample during the measurement.

X-ray photoelectron spectra (XPS) were recorded on a Kratos Axis Ultra DLD (Kratos Analytical, Manchester, U.K.), using monochromatic Al K $\alpha$  line (1486.69 eV) with X-ray power of 150 W. Survey spectra were collected with a 160 eV pass energy, while core-level scans were collected with a pass energy of 20 eV. The pressure in the system was 266.64 × 10<sup>-9</sup> Pa. The analysis area for the data collection using the hybrid electrostatic and magnetic lens system and the slot aperture was approximately 300 × 700 mm<sup>2</sup>. Data analysis was performed with CasaXPS using Kratos relative sensitivity factors. Core-level scans were calibrated based on a peak fit to the C 1s scan, with the component due to aromatic carbon set to 284.7 eV. Shirley backgrounds were used throughout. Gaussian–Lorentzian product line-shapes were used with a 30% Lorentzian weighting.

The elemental microanalysis (C, H, and N; O was determined from the difference) was carried out using the Elemental Analyzer Vario EL III (Elementar).

The content of Fe in the samples was determined by inductively coupled plasma optical emission spectroscopy (ICP-OES), using a Thermo Scientific iCAP 6500 Duo ICP spectrometer. Prior to analysis by ICP-OES, the microwave-assisted acid digestion of samples was performed by means of ETHOS 1 Advanced Microwave Digestion System (Milestone, Italy) using HPR-1000/10S high-pressure segmented rotor. The acid mixture consisting of 65% HNO<sub>3</sub> (2 cm<sup>3</sup>) and 96% H<sub>2</sub>SO<sub>4</sub> (6 mL) was used for the acid digestion per ~25 mg of the sample. ICP-OES analysis was performed using an emission line of Fe II 240.488 nm.

Nitrogen physisorption analysis was performed by nitrogen adsorption at 77 K using a Sorptomatic 1990 Thermo Finnigan device. Prior to adsorption, the samples were degassed for 1 h at room temperature under vacuum and for a further 16 h at 383 K at the same residual pressure. Software ADP, version S.13 CE Instruments was used to analyze the resulting nitrogen-adsorption isotherms.

**Electrochemical Measurements.** Electrochemical measurements of investigated PPy-NT and C-PPy-NT samples were

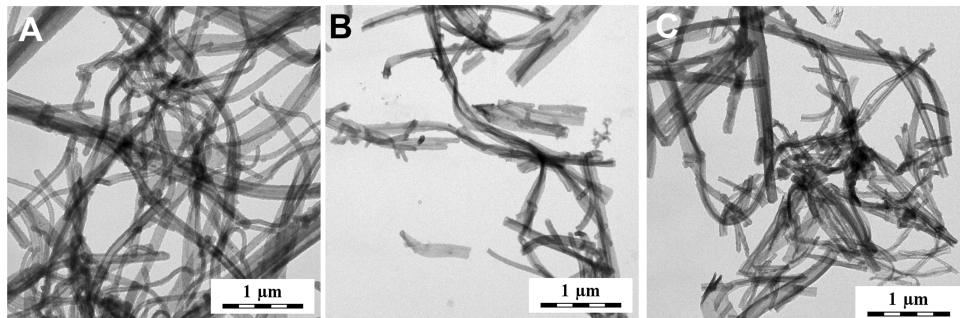


**Figure 1.** TEM micrographs of PPy-NT salt (A), PPy-NT base (B), and C-PPy-NT produced by carbonization of PPy-NT salt (C).

performed at room temperature using a Gamry PCI4/750 potentiostat–galvanostat (Gamry, U.S.). A conventional one-compartment three-electrode electrochemical cell was used with a saturated calomel electrode (SCE) and a large platinum plate as the reference and counter electrode, respectively. Chemicals used in this study were of analytical purity grade purchased from Sigma-Aldrich and were used without further purification. Gases ( $N_2$ ,  $O_2$ ) were of high purity (99.999 vol %, Messer). The working electrode was PPy-NT or C-PPy-NT-modified glassy carbon (GC) disk electrode (base surface area,  $0.196\text{ cm}^2$ ) mounted to a Pine rotator. Electrode preparation is described below.

For the electrochemical measurement of PPy-NT base and PPy-NT salt, 4.0 mg of each sample was mixed with a 1.0 mg Vulcan XC-72 carbon black (Cabot, U.S., 50 nm spherical particles) and suspended in 1.0 mL of water–ethanol mixture (3:2 by volume) using an ultrasonic bath. Then, 10  $\mu\text{L}$  of the suspension was transferred onto the GC disk and the solvent was evaporated under a nitrogen stream. After drying, thin sample layer was covered with 10  $\mu\text{L}$  of 0.05 wt % solution of Nafion ionomer in ethanol, and the ethanol was allowed to evaporate off. Vulcan XC-72 was added to serve as a current collector, while Nafion ensured attachment of the sample layer to the GC surface, which is necessary for good electrical contact. The electrodes prepared by this method were transferred to the electrochemical cell containing nitrogen-purged 1 M potassium chloride solution. Cyclic voltammetry measurements were performed for these two samples to assess their capacitive behavior.

Electrode preparation for the case of C-PPy-NT sample was performed in the same manner. Because of good conductivity of C-PPy-NT, however, a total mass of 5.0 mg of this material was dispersed in water–ethanol mixture without addition of carbon black. Capacitive behavior of C-PPy-NT was investigated using cyclic voltammetry in nitrogen-purged 6 M aqueous potassium hydroxide solution while ORR was probed using rotating-disk electrode (RDE) voltammetry in oxygen-saturated 0.1 M aqueous potassium hydroxide solution.

## RESULTS AND DISCUSSION

**Morphology.** The inspection of TEM micrographs reveals nanotubular morphology of all samples (Figure 1). Samples are composed entirely of nanotubes with an outer diameter between  $\approx 70$  and 300 nm. The lengths of the nanotubes are up to several micrometers. Most importantly, morphological features of PPy-NT salt were retained after carbonization, in agreement with previous reports on different nanostructured PPy.<sup>46,65</sup>

**FTIR Spectra: Polypyrrole Salt.** Absorption of the PPy-NTs as-produced salt was very small, and the measured spectra contained relatively strong absorption bands in the region of stretching and bending vibrations of water molecules at about 3436 and 1634  $\text{cm}^{-1}$ , respectively (Figure 2). This is caused by

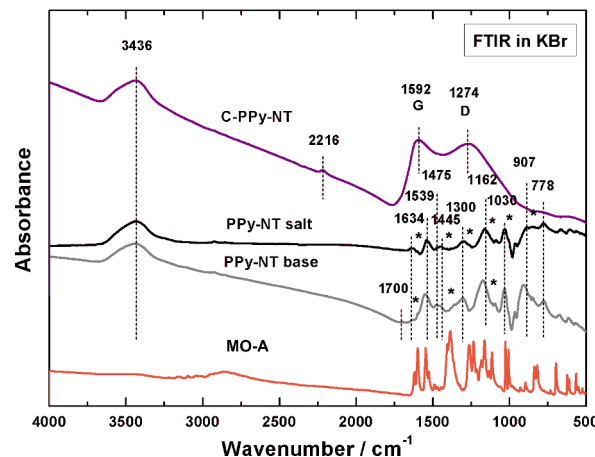


**Figure 2.** FTIR spectra of original PPy-NT salt and product of its carbonization (C-PPy-NT). Spectra of the corresponding PPy-NT base and of methyl orange acid (MO-A) are included.

its compact stone-like structure which was difficult to disperse in potassium bromide pellets. After deprotonation to PPy-NT base, the sample was much better dispersible in the pellets. The infrared spectrum of PPy-NT salt contains the main bands of PPy described earlier.<sup>66,67</sup> The band at 1539  $\text{cm}^{-1}$  is assigned to C–C stretching vibrations in the pyrrole ring, and the band at 1445  $\text{cm}^{-1}$  (with a shoulder at 1475  $\text{cm}^{-1}$ ) to the C–N stretching vibration in the ring. The broad band with maximum at about 1300  $\text{cm}^{-1}$  is attributed to C–H or C–N in-plane deformation modes, and a maximum at 1162  $\text{cm}^{-1}$  (influenced by the overlap with the band of methyl orange) is observed in the region of the C–H and N–H in-plane deformation vibrations. The band at 1030  $\text{cm}^{-1}$  corresponds to the C–H and N–H in-plane deformation vibrations, and the peaks at about 900 and 778  $\text{cm}^{-1}$  to the C–H out of plane deformation vibrations of the ring.

After detailed analysis of the spectrum, we can detect the presence of the peaks of methyl orange (MO) marked with asterisks in Figure 2. Comparing the positions of these peaks with the spectrum of MO, we can conclude that it is present in the composite in the acid form MO (Figure 2). Infrared spectra of MO in various situations are shown in Figure 3. Peaks of MO observed in the infrared spectra of PPy-NTs correspond

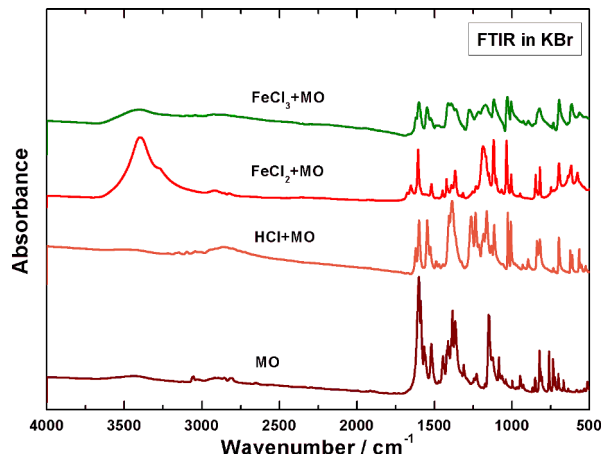


Figure 3. FTIR spectra of methyl orange in various stages.

most probably to the solid precipitated structures which are produced when MO interacts with iron(III) salts.<sup>63</sup> Such objects are likely to act as templates in the growth of PPy-NTs.<sup>64</sup>

**FTIR Spectra: Polypyrrole Base.** The spectrum of PPy-NT base differs from the spectrum of the original PPy-NT salt (Figure 2). The maxima of the bands observed in the spectrum of the salt at about 1539, 1162, and 900 cm<sup>-1</sup> are slightly shifted to higher wavelengths 1553, 1173, and 909 cm<sup>-1</sup>, and a weak band at 1700 cm<sup>-1</sup>, which corresponds to the presence of carbonyl group formed by the nucleophilic attack of water during the preparation, can be observed.<sup>66,67</sup> The peaks of MO are still detected in the spectrum of PPy-NT base (Figure 2), i.e., MO was not removed after the deprotonation, and a strong interaction between MO and PPy occurs. This means that MO always constitutes a part of the samples.

**FTIR Spectra: Carbonized Material.** In the FTIR spectrum of C-PPy-NT salt (Figure 2), we observe a local maximum at 1592 cm<sup>-1</sup> and a broad band with the maximum at about 1274 cm<sup>-1</sup>. The first band emerged from the C–C stretching vibrations in the pyrrole ring, and the second from the C–N in-plane deformation modes.<sup>66,67</sup> The shape of the spectrum is close to that of the spectra of a carbon-like material with the Raman-active D (disordered) and G (graphitic) bands (see below), which are usually inactive in FTIR spectra. In disordered samples, however, they become IR-active because of symmetry-breaking of the carbon network, but they are rather weak and the spectra are flat and almost featureless.<sup>46</sup> The spectrum of C-PPy-NT salt illustrates the complete conversion of molecular structure of PPy to a nitrogen-containing carbon.

**Raman Spectra: Polypyrrole Salt.** Raman spectroscopy is well-suited to characterize the progress of carbonization (Figure 4). Because of the resonant enhancement of the scattered light it is also a suitable method for detecting small amount of additives, such as methyl orange. Raman spectra measured with an excitation wavelength of 785 nm, which is not in resonance with methyl orange, display clearly the spectral features of PPy. On the contrary, the Raman spectra of PPy-NT salt and base recorded with 514 nm excitation wavelength displayed mostly the spectral features of methyl orange, thus confirming its presence in the samples.

The Raman spectrum of as-produced PPy-NTs measured with a 785 nm excitation laser (Figure 4a) displays bands typical of PPy salt<sup>68–72</sup> (Table 1). There are, however, several deviations from the spectrum of globular PPy prepared in the

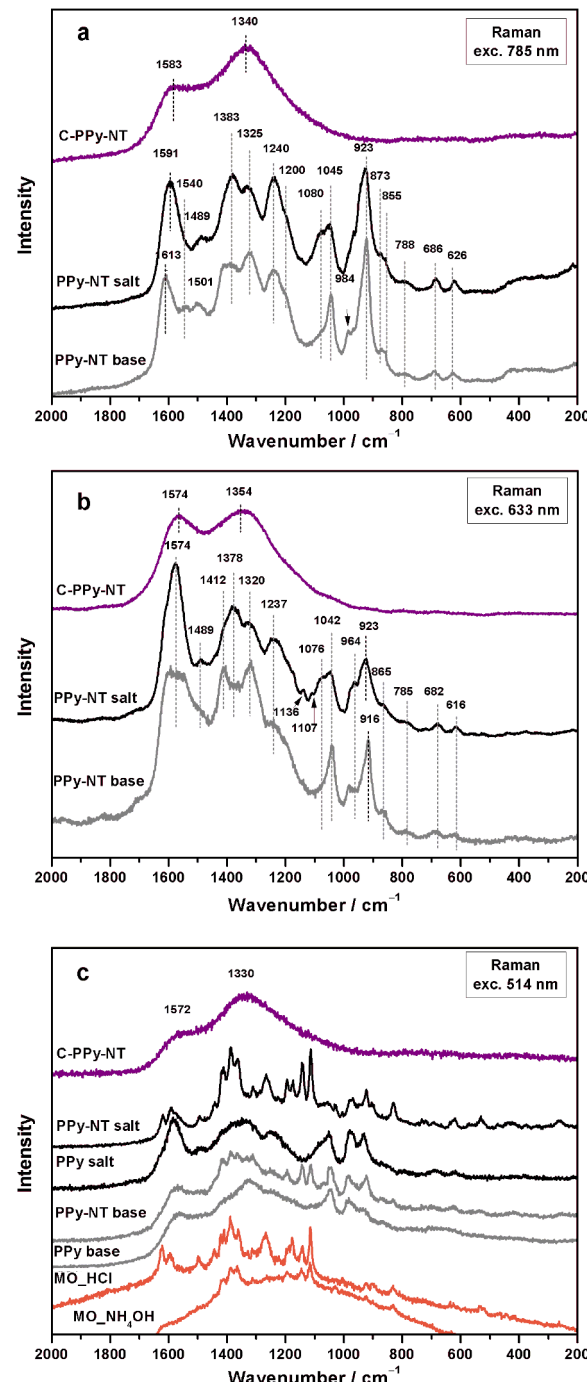


Figure 4. Raman spectra of original PPy-NT salt and product of its carbonization (C-PPy-NT) and spectra of the corresponding PPy-NT base measured with 785 (a), 633 (b), and 514 nm (c) laser excitation lines. Raman spectra of acidic (MO\_HCl) and basic (MO\_NH<sub>4</sub>OH) forms<sup>64</sup> of methyl orange salt, globular PPy salt, and PPy base (prepared without methyl orange) measured with 514 nm (c) laser excitation are shown for comparison.

absence of MO. The bands at 923 and 1045 cm<sup>-1</sup> are shifted to lower wavenumbers, and they are more intense (940 and 1056 cm<sup>-1</sup> for granular PPy). The band at 1325 cm<sup>-1</sup> is stronger, and the band at 1591 cm<sup>-1</sup> is weaker; the small peaks at 855 and 788 cm<sup>-1</sup> are well-developed. When recorded with a 633 nm excitation laser (Figure 4b), the spectral features of PPy-NT salt are close to those of granular PPy salt. Only small peaks connected with methyl orange appear at 1136 and 1107 cm<sup>-1</sup>,

**Table 1.** Assignment of the Raman Bands of PPy-NT Salt and Base Measured with 785 and 633 nm Excitation Lasers<sup>a,68–72</sup>

785 nm		633 nm		assignment
salt	base	salt	base	
—	1613 s	—	—	$\nu(C=C)$ in the dication pyrrole ring
1591 s		1574 s	1574 s	ring $\nu$ of neutral and radical cation units
—	1540 w	—	—	$\nu(\text{ring})$
1489 w	1501 w	1489 w	1489 sh	$\nu(C=N)$ and $\nu(C-C)$
—	—	1412 sh	1412 s	$\nu(C-C)$ and $\nu(C-N)$
1383 s	1383 s	1378 m	—	$\delta(C-H)$ and $\delta(N-H)$ , $\nu(C-C)$ of neutral units
1325 s	1325 s	1320 m	1320 s	$\nu(C-C)$ of neutral units
1240 s	1245 s	1237 m	1237 m	antisymmetric $\delta(C-H)$
1200 sh	1200 sh	—	—	antisymmetric $\delta(C-H)$
—	—	1136 w	—	methyl orange
—	—	1107 w	—	methyl orange
1080 m	1080 sh	1076 m	—	$\gamma(C-H)$ , $\gamma(N-H)$ and ring $\gamma$
1045 m	1045 m	1042 m	1042 m	$\delta(C-H)$ , $\delta(N-H)$ and ring $\delta$ in radical cation units
984 sh	984 w	964 m	964 w	$\delta(C-C)$ in radical cation and neutral units
923 s	923 s	923 m	916 m	$\delta(\text{ring})$ in dication units
873 sh	873 w	865 sh	865 w	$\delta(\text{ring})$
855 sh	855 w	—	—	$\gamma(C-H)$
788 w	788 w	785 w	785 w	$\gamma(C-H)$
686 w	686 w	682 w	682 w	$\gamma(\text{ring})$
626 w	626 w	616 w	616 w	torsion of the ring

<sup>a</sup>Abbreviations: s, strong; m, medium; w, weak; sh, shoulder;  $\nu$ , stretching;  $\delta$ , in-plane bending;  $\gamma$ , out-of-plane deformation; B, benzenoid ring; Q, quinonoid ring; SQ, semiquinonoid ring; Phz, phenazine-like segment; ~, a bond intermediate between a single and a double bond; o.p., out-of-plane; i.p., in plain.

and the peaks at 923 and 1574  $\text{cm}^{-1}$  are shifted to smaller wavenumbers (from 930 and 1588  $\text{cm}^{-1}$ ). The Raman spectrum of PPy-NT salt measured with a 514 nm excitation laser (Figure 4c) is overwhelmed with the spectral features of the acidic form of methyl orange (Figure 4c). The fluorescence background of methyl orange is absent in the spectrum, and the interaction of methyl orange with PPy  $\pi$ -conjugated system is a possible cause. However, methyl orange alone does not always display strong fluorescence, as in the case of the spectrum shown.

**Raman Spectra: Polypyrrole Base.** The Raman spectrum of PPy-NT base measured with a 785 nm excitation laser (Figure 4a) displays the same differences in the comparison with the Raman spectrum of granular PPy measured with this excitation in the salt form. In addition, a weak band at 1540  $\text{cm}^{-1}$  is observed. In the Raman spectrum of PPy-NT base measured with a 633 nm excitation laser (Figure 4b, Table 1) there are more pronounced deviations from the spectrum of granular PPy. The band at 1574  $\text{cm}^{-1}$  is weaker and shifted slightly to lower wavelengths (from 1588  $\text{cm}^{-1}$ ). The band at 1378  $\text{cm}^{-1}$  is missing. The peak at 916  $\text{cm}^{-1}$  is shifted to lower wavenumbers (from 930  $\text{cm}^{-1}$ ), and the band at 964  $\text{cm}^{-1}$  is weaker. The Raman spectrum of PPy-NT base recorded with a 514 nm excitation laser (Figure 4c) displays sharp bands of the basic form of methyl orange (MO) on the broad bands of PPy base (both spectra are shown in Figure 4c for comparison). The fluorescence background of methyl orange is again missing.

**Raman Spectra: Carbonized Polypyrrole.** The carbonization of PPy is associated with dramatic changes in molecular structure that are reflected in Raman spectra. In the Raman spectrum of C-PPy-NT measured with a 785 nm excitation laser (Figure 4a), the band at 1583  $\text{cm}^{-1}$  (emerging from the C=C stretching vibrations of the pyrrole ring) and the broad band centered at 1340  $\text{cm}^{-1}$  (emerging from the C-C stretching of the pyrrole ring) are observed. These bands can

be considered to be G-band (“graphitic” band, C=C stretching of any pair of  $\text{sp}^2$  sites) and D-band (“disorder” band, breathing of aromatic rings activated by any defect including a heteroatom) defined for graphitic material<sup>73</sup> and proven to be usable for nitrogen-doped carbonaceous material.<sup>74</sup> The spectrum corresponds to the disordered nitrogen-containing graphitic material.<sup>75</sup> The D/G intensity ratio, determined by intensities at band maxima (baseline-corrected spectra were used), is 1.4. In the Raman spectrum of C-PPy-NT measured with a 633 nm excitation laser (Figure 4b), we can observe the G-band at 1574  $\text{cm}^{-1}$  and the D-band at 1354  $\text{cm}^{-1}$ . The position shifts and the intensity change of these bands with the change of excitation wavelength are due to the resonance effect in graphite-like materials. The D/G intensity ratio is 1.5. In the Raman spectrum of C-PPy-NT measured with 514 nm excitation laser (Figure 4c), the G-band is located at 1572  $\text{cm}^{-1}$  and the D-band at 1330  $\text{cm}^{-1}$ . The D/G intensity ratio is 2. The Raman spectra thus confirm the complete conversion of PPy to a nitrogen-enriched carbon.

**Conductivity.** Conductivity of the prepared C-PPy-NT sample is in line with previous reports.<sup>46</sup> Conductivities of PPy-NT salt and PPy-NT base samples differ from each other by 2 orders of magnitude, the former one being better the conductor (Table 2). On the other hand, upon carbonization, conductivity of PPy-NT salt is reduced by about 1 order of magnitude. As a

**Table 2.** Conductivity of PPy-NT Salt and Base and C-PPy-NT (Produced by Carbonization of PPy-NT Salt) Measured at Two Different Pressures

pressure (MPa)	conductivity ( $\text{S cm}^{-1}$ )		
	PPy-NT salt	PPy-NT base	C-PPy-NT
125	1.0	0.016	0.07
500	0.9	0.039	0.12

**Table 3.** Elemental Composition of PPy-NT Salt and Base and C-PPy-NT (Produced by Carbonization of PPy-NT Salt), Determined by the Elemental Microanalysis and ICP-OES (wt %) and the Results of XPS Analysis (atom %)

element	PPy-NT salt		PPy-NT base		C-PPy-NT	
	elemental composition (wt %)	XPS (atom %)	elemental composition (wt %)	XPS (atom %)	elemental composition (wt %)	XPS (atom %)
N	16.18	14.0	16.90	13.3	14.87	11.6
O	20.16 <sup>a</sup>	7.2	17.84 <sup>a</sup>	9.7	13.70 <sup>a</sup>	7.0
C	56.68	74.6	58.85	75.9	69.36	81.3
Cl	—	3.0	—	0.3	—	—
S	2.28	1.0	1.88	0.8	—	—
H	4.67	—	4.48	—	2.02	—
Fe	0.032 <sup>b</sup>	0.2	0.055 <sup>b</sup>	0	0.049 <sup>b</sup>	0.06

<sup>a</sup>Estimated indirectly on the basis of N, C, S, Cl, and H weight fraction (from the results of the elemental microanalysis) and weight fraction of Fe (determined by ICP-OES). Also includes weight fraction of Cl. <sup>b</sup>ICP-OES result.

comparison, this carbonized sample is slightly less conductive than previously investigated nanostructured carbonized polyaniline with a high contribution of nanotubes and/or nanorods.<sup>16,51,52,76</sup> It should be noted that for the two less conductive samples, PPy-NT base and C-PPy-NT, measured conductivities show pronounced dependence on the applied pressure, being higher as applied pressure increased. This can be understood as an effect of tighter packing of particles and formation of better and larger (in terms of total area) electrical contact at higher pressures, which is significant if the material is not highly conducting. The conductivity of PPy-NT salt compressed into a pellet was reported<sup>64</sup> to be 40–70 S cm<sup>-1</sup>; the carbonized material could not be compressed in a similar manner.

**XPS and Elemental Analysis.** The determining role of nitrogen-containing surface groups for efficient ORR electrocatalysis in nitrogen-doped carbon materials has been well-established.<sup>77,78</sup> However, there is still an ongoing debate about the role and importance of various surface nitrogen functional groups in ORR catalysis.<sup>79–82</sup> Additionally, charge-storage behavior of nitrogen-doped carbon materials is, among other parameters, strongly dependent on the bulk and surface content of nitrogen and oxygen atoms and on the types of heteroatom-containing surface functional groups. With this in mind, we have performed XPS measurements and elemental analysis to assess elemental composition and surface chemistry of investigated materials, which is also linked with electrochemical performance.

Taking into account the fact that XPS determines the surface elemental composition while elemental analysis provides the overall elemental composition, results of elemental analysis and XPS analysis (Table 3) indicate that prepared PPy samples have high carbon content with significant contributions of O and N. Also, Cl, S, and H are present to a certain extent. However, one should keep in mind that elemental microanalysis can provide data only on the N, C, S, and H content, while the weight fraction of the other elements (usually oxygen) are determined by physical and chemical reasoning on the basis of the nature of the investigated material. On the other hand, XPS analysis cannot provide hydrogen mole fraction, which can be very high, even though its mass fraction is low because of small atomic weight. Hence, direct comparison of the results provided by elemental microanalysis and XPS is not as straightforward as might be expected. When the elemental microanalysis results for the three analyzed samples (Table 3) are compared, it is clear that elemental compositions of PPy-NT salt and PPy-NT base are rather similar. However, a significant change of the elemental composition of the PPy-NT salt is seen upon

carbonization: while C content increased significantly, the content of the other elements initially present in the sample is reduced. The same can be concluded regarding materials surface composition, as seen by XPS. A rather high nitrogen surface content of 11.6 atom % is observed in C-PPy-NT. Having in mind the notes given above on the correspondence between the results of elemental microanalysis and XPS, it is relatively safe to disregard H content when transforming mole composition of C-PPy-NT (obtained by XPS) to weight fractions for the purpose of direct comparison of the results provided by these two methods. If this is done, surface weight composition of N, O, and C in C-PPy-NT is 13.1, 8.9, and 78.0 wt %, in that order. This means that, upon carbonization, the surface gets depleted in N and O (more pronouncedly than N), while C surface content increases significantly. On the basis of this observation, a core–shell structure of C-PPy-NT can be expected, similar to that observed for carbonized polyaniline (PANI).<sup>83</sup> Shell and core are differentiated by the degree of carbonization, the shell being more carbonized than the core.

Several surface oxygen and nitrogen groups were identified by deconvolution of their respective O 1s and N 1s high-resolution XPS signals (Figures 5 and 6). O 1s peaks appear at binding energies of 531.1 and 532.5 eV for PPy-NT salt and at 531.3 and 532.9 eV for PPy-NT base. The peak at 531.1/531.3 eV can be attributed to the oxygen present in the  $-\text{SO}_3$  group in MO<sup>84</sup> with possible contribution of C=O groups, while the peak at 532.5/532.9 eV corresponds to C–OH hydroxyl groups (Table 4).<sup>15,83</sup> The carbonyl and hydroxyl groups are common structural defects in PPys. Because sulfur (and the  $-\text{SO}_3$  group) is not present in the material upon the carbonization, the O 1s peak of C-PPy-NT at 530.8 eV is assigned only to C=O groups. The peak due to C–OH hydroxyl groups and/or  $-\text{COOH}$  carboxyl groups is observed at 532.6 eV upon carbonization (Table 4).

Binding energies at 397.7 and 398.1 eV for the PPy-NT salt and base, respectively, are attributed to uncharged imine nitrogen,<sup>85</sup> while the peak at a similar position of 398.3 eV in the spectrum of C-PPy-NT originates from pyridinic nitrogen (N-6).<sup>15,86</sup> Pyrrolic nitrogen (N-5) is revealed by the peak at about 400.0 eV in all the samples.<sup>15</sup> Noncarbonized PPy-NT samples also exhibit the peak at 401.3 eV (salt form) and 401.8 eV (base form) which can be ascribed to protonated (charged) nitrogen and high oxidation states of nitrogen atoms.<sup>85</sup> This peak is not detected for C-PPy-NT, indicating the absence of quaternary nitrogen which was previously reported in some works on carbonized PPY.<sup>85</sup> Estimates of the individual nitrogen and oxygen species fractions are based on the area of their respective XPS peaks. On the basis of the contribution

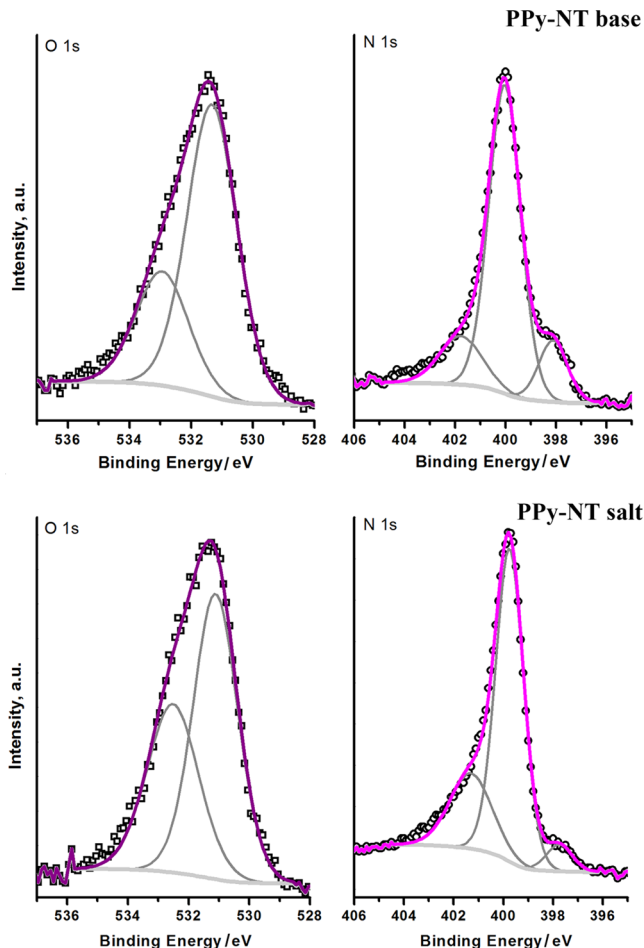


**Figure 5.** Deconvoluted O 1s (left panels) and N 1s (right panels) high-resolution XPS signals of PPy-NT base (top panels) and PPy-NT salt samples (bottom panels).

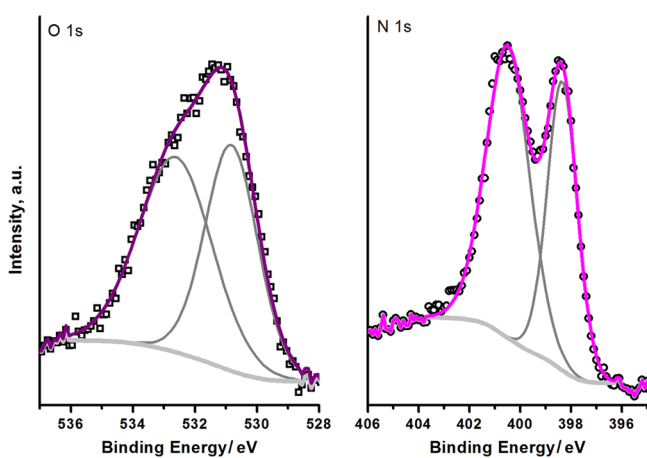


**Figure 6.** Deconvoluted O 1s (left panel) and N 1s (right panel) high-resolution XPS signals of C-PPy-NT produced by carbonization of PPy-NT salt.

of individual nitrogen group type to the overall surface concentration, it can be concluded that uncharged pyrrolic nitrogen atoms are the dominant surface nitrogen species in noncarbonized PPy samples, with around 70 atom % N forming this moiety. The content of uncharged imine nitrogen is higher in PPy-NT base than in PPy-NT salt, as expected, due to the

deprotonation,<sup>63</sup> while the content of charged imine nitrogen in PPy-NT salt is higher than that in PPy-NT base. Interestingly, C-PPy-NTs have nitrogen atoms only in pyridinic (N-6) and pyrrolic/pyridone (N-5) form, which are approximately equally abundant. This can be envisioned as a transformation of pyrrolic form to pyridinic nitrogen. Similar transformations upon heating the carbon samples can be found in the literature.<sup>83,85,87</sup>

**Textural Properties.** The specific surface area and pore structure are assumed to be crucial for good capacitive performance. To obtain textural parameters, the samples were subjected to the nitrogen adsorption–desorption measurements (Figure 7, Table S). There is a distinct difference between PPy-NT base and PPy-NT salt on one hand and the C-PPy-NT on the other, so they should be viewed separately.

Noncarbonized PPy-NT samples have relatively low specific surface area  $S_{\text{BET}}$  values of around  $55 \text{ m}^2 \text{ g}^{-1}$ . The shape of their isotherms together with low  $S_{\text{BET}}$  and low value of constant C from BET isotherms (48.2 for PPy-NT salt and 57.5 for PPy-NT base) indicate low overall porosity of these materials. Also, the absence of hysteresis loop as well as small positive slope in the region of relative pressures which corresponds to mesopores clearly indicate low amounts of mesopores in both PPy-NT samples. For both materials, the isotherms are Type II according to IUPAC classification.<sup>88</sup> Clear effect of carbonization can be recognized on the isotherm of C-PPy-NT. In low relative pressure region (below 0.17), large increase of adsorbed nitrogen volume can be observed, which means the development of microporosity during carbonization. Also, an obvious hysteresis loop emerged, giving evidence of the presence of a significant amount of mesopores in C-PPy-NT. Upon carbonization,  $S_{\text{BET}}$  drastically increased to  $257 \text{ m}^2 \text{ g}^{-1}$ . Overall, all textural parameters increase, and the isotherm of C-PPy-NT is a combination of type I in the region of low pressures and type II in the region of high pressures.

**Electrochemistry of PPy-NT Base and PPy-NT Salt.** Capacitive behavior of PPy-NT base and PPy-NT salt samples, probed in 1 M potassium chloride solution (Figure 8) points to distinct electrochemical behavior of these materials. Cyclic voltammograms of PPy-NT base (Figure 8, left panels) display wide anodic peaks centered around 0 V versus SCE, similar to some of the previously reported PPy cyclic voltammograms at the same pH.<sup>93,94</sup> In contrast, cyclic voltammograms of PPy-NT salt are close to ideal capacitor  $I$ - $E$  characteristics, being rectangular in shape (Figure 8, right panels).

In addition, even more interesting differences between PPy-NT salt and PPy-NT base were observed when dependence of gravimetric capacitance of these two materials on the potential sweep rate was investigated (Figure 8, middle panel). In the case of PPy-NT base, the gravimetric capacitance at low potential sweep rate ( $5 \text{ mV s}^{-1}$ ) is around  $140 \text{ F g}^{-1}$ , while it decays abruptly upon increasing potential sweep rate to  $40 \text{ F g}^{-1}$  at  $100 \text{ mV s}^{-1}$ . In the case of PPy-NT salt, the gravimetric capacitance was found to be practically independent of the potential sweep rate with a value around  $115 \text{ F g}^{-1}$  for the potential sweep rate between  $5$  and  $100 \text{ mV s}^{-1}$ . According to the overview provided by Ramya et al.,<sup>95</sup> the values of gravimetric capacitance of both PPy-NT base and PPy-NT salt at low potential sweep rates agree well with previously reported values for different PPy samples, although capacitances as high as  $556 \text{ F g}^{-1}$  were reported for PPy-based composites.<sup>96</sup>

Double-layer charging of small surface areas of PPy-NT base and salt cannot solely account for high capacitance values.

**Table 4.** XPS Peak Positions (Binding Energy, BE) and Relative Content of Oxygen and Nitrogen Species in Studied Samples<sup>a</sup>

oxygen species	PPy-NT salt		PPy-NT base		C-PPy-NT	
	BE (eV)	% O atoms	BE (eV)	% O atoms	BE (eV)	% O atoms
C=O					530.8	45.4
O in $-\text{SO}_3^-$ , C=O	531.1	59.5	531.3	70.8		
C-OH	532.5	40.5	532.9	29.2		
C-OH, -COOH					532.6	54.6
nitrogen species	PPy-NT salt		PPy-NT base		C-PPy-NT	
	BE (eV)	% N atoms	BE (eV)	% N atoms	BE (eV)	% N atoms
uncharged imine N	397.7	5.5	398.1	13.0		
pyridinic nitrogen (N-6)					398.3	40.4
pyrrolic nitrogen (N-5)	399.8	69.3	400.0	71.8	400.5	59.6
protonated (charged) N/ high oxidation states of N	401.3	25.1	401.8	15.0	—	—

<sup>a</sup>Estimation of nitrogen species fraction is based on the area of their respective peaks.

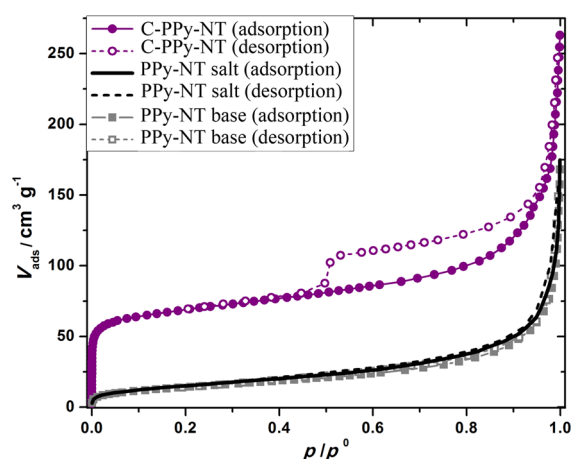


**Figure 7.** Nitrogen adsorption–desorption isotherms of PPy-NT base (squares), PPy-NT salt (dark full and dashed line), and C-PPy-NT produced by carbonization PPy-NT salt (circles).

**Table 5.** Textural Properties of Investigated Materials: Mesopore Volume ( $V_{\text{meso}}$ ), Mesopore Surface Area ( $S_{\text{meso}}$ ), Micropore Volume ( $V_{\text{micro}}$ ), and Specific Surface Area ( $S_{\text{BET}}$ ).<sup>89</sup> Particular Methods for Determination of These Properties Are Denoted as DH, Dollimore–Heal;<sup>90</sup> HK, Horwath–Kawazoe;<sup>91</sup> and DR, Dubinin–Radushkevich<sup>92</sup>

	characteristic	PPy-NT base	PPy-NT salt	C-PPy-NT
mesopores	$V_{\text{meso}}$ (DH) ( $\text{cm}^3 \text{g}^{-1}$ )	0.100	0.103	0.167
	$S_{\text{meso}}$ (DH) ( $\text{m}^2 \text{g}^{-1}$ )	44.6	49.8	86.2
micropores	$V_{\text{micro}}$ (HK) ( $\text{cm}^3 \text{g}^{-1}$ )	0.021	0.023	0.105
	$V_{\text{micro}}$ (DR) ( $\text{cm}^3 \text{g}^{-1}$ )	0.017	0.019	0.099
specific surface area	$S_{\text{BET}}$ ( $\text{m}^2 \text{g}^{-1}$ )	52.8	57.0	257.3

Similar behavior of different nitrogen-containing carbons is explained by the significant contribution of pseudocapacitance provided by nitrogen and oxygen functionalities.<sup>97,98</sup> We suspect that this is the case here, as XPS data point to high surface content of nitrogen groups active for pseudocapacitance. Cyclic voltammetric measurements support this conclusion as voltammograms display typical features of pseudocapacitive charging, namely the broad current hump between  $-0.4$  and  $0.3$  V.

A frequently overlooked property of carbon-based materials (or in general different electrode materials) is their

conductivity. It has been shown that, besides surface functional groups and adequate porosity, conductivity plays a major role in carbon-based capacitors.<sup>99,100</sup> Studies have shown that the carbonization process can lead to an increase in conductivity of 6–8 orders of magnitude.<sup>101</sup> However, in the present case, a certain decrease in conductivity was observed upon carbonization of PPy-NT salt (Table 2). On the other hand, conductivities of two noncarbonized PPy-NT samples differ by 2 orders of magnitude. In fact, the difference in the conductivity of these two samples appears to be the parameter which differentiates them, as textural features and surface chemistry of these two samples are basically the same. We suspect that difference in conductivity of PPy-NT base and PPy-NT salt, being 2 orders of magnitude, can explain (1) the same initial capacitance and (2) a significant capacitance fade upon increasing potential sweep rate for the PPy-NT base sample. The electrodes were prepared in the same manner, and it is assumed that the interfacial region between the current collector (Vulcan XC-72) and the active material is the same in both cases. This is, however, obviously not sufficient in the higher potential sweep rate regimes. We believe that the present results are one of the most straightforward proofs regarding the crucial role of the material's conductivity in the capacitive performance. It is proposed that, for the low-conducting sample, the electron mobility is hindered and that, in the high potential sweep rate regime, a double-layer charging is restricted to the part of the material surface close to the Vulcan–(active material) boundary region. When the time scale of the potential cycling experiment is extended (upon reduction of potential sweep rate), enough time is provided for double-layer charging over extended parts of the material surface, resulting in tremendous increase in gravimetric capacitance. High conductivity of PPy-NT salt sample does not allow for the observation of the effects of hindered electron transport within the time frames of typical electrochemical experiment in which material capacitance is evaluated. Hence, constant capacitance was observed, which does not depend on the potential sweep rate.

**Electrochemistry of C-PPy-NTs.** C-PPy-NTs displayed gravimetric capacitance between  $220 \text{ F g}^{-1}$  ( $5 \text{ mV s}^{-1}$ ) and  $120 \text{ F g}^{-1}$  ( $100 \text{ mV s}^{-1}$ ), as assessed by cyclic voltammetry in 6 M potassium hydroxide solution (Figure 9, top panels). Gravimetric capacitance was found to decrease in a linear manner with a logarithm of potential sweep rate (Figure 9, bottom panel). As reviewed recently,<sup>46</sup> these results are similar

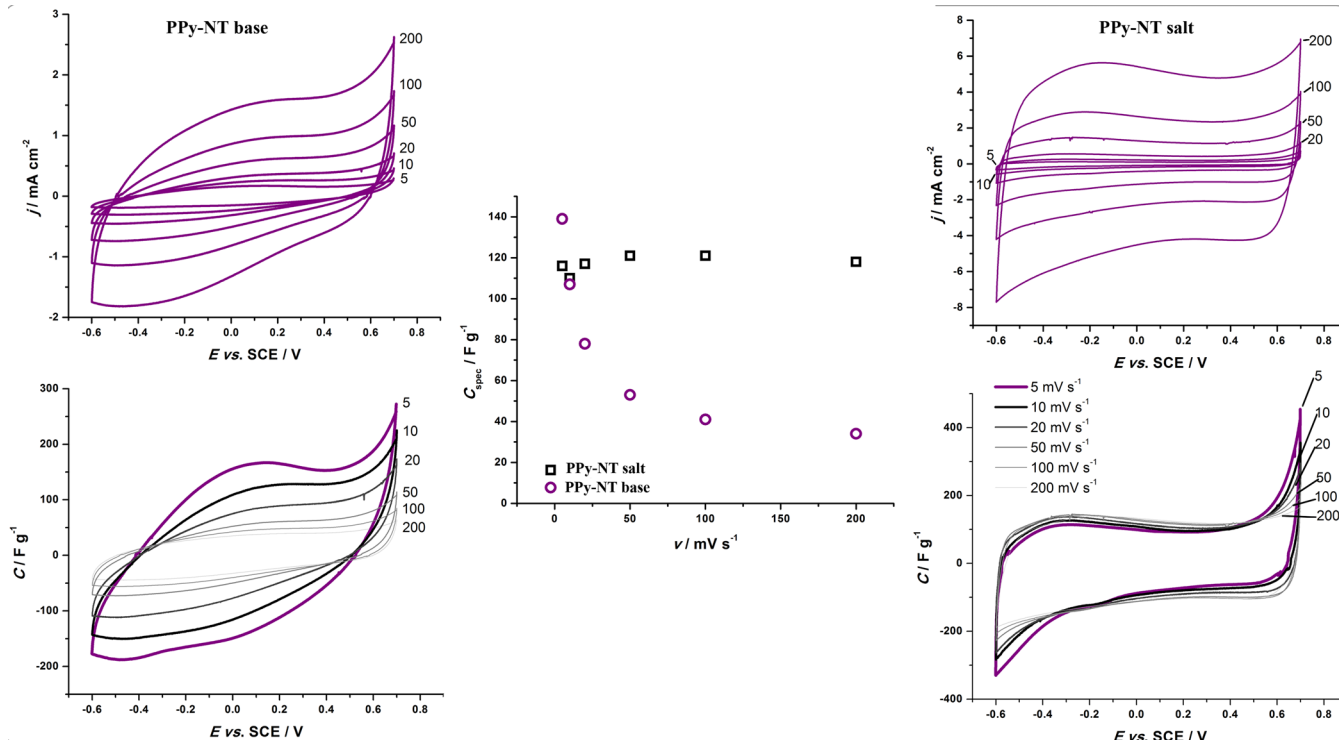


**Figure 8.** Recorded cyclic voltammograms for PPy-NT base sample at different potential sweep rates (top left panel) along with cyclic voltammograms normalized by potential sweep rate and the mass of the material to assess material's gravimetric capacitance (bottom left panel). The same is provided for PPy-NT salt sample on the right-hand side. In the middle panel, the dependence of PPy-NT base (○) and PPy-NT salt (□) gravimetric capacitance on the potential sweep rate is provided.

to previously reported values, but some higher values could also be found in the literature for the materials developed specifically for charge-storage applications.<sup>83</sup> In a very recent paper, Zhou et al.<sup>102</sup> reported capacitance values of 272.0 F g<sup>-1</sup> (5 mV s<sup>-1</sup>) and 105.1 F g<sup>-1</sup> (100 mV s<sup>-1</sup>) for a very similar material, in 1 M sulfuric acid, which demonstrated somewhat higher capacitance fade compared to that of C-PPy-NTs presented here. Upon activation, about 50% increase in capacitance was obtained with significantly improved capacitance retention, which was attributed to an enlarged surface area and higher O/C and N/C surface ratios. It is expected that gravimetric capacitances found here for C-PPy-NT could be significantly improved using some of the activation procedures reported in the literature.<sup>83,103</sup> Normalized cyclic voltammograms of C-PPy-NT all show broad current maximum between -1.0 and -0.7 V versus SCE, which is indicative of the occurrence of pseudocapacitive reactions. This behavior is expected because of the high surface nitrogen content as evidenced by XPS measurements. It should be noted that redox reactions of nitrogen surface functional groups are not as prominent as those being observed in some cases of N-containing carbon materials. For example, Wang et al.<sup>104</sup> clearly demonstrated redox processes of N-functional groups for N-doped carbon monolith. Following the aforementioned work and on the basis of XPS data (only N-6 and N-5 nitrogen present, Table 4), it can be concluded that pseudofaradaic processes of N-containing functional groups which contribute to overall capacitance are (i) two-electron conversion of pyridinic (N-6) nitrogen to pyridone form of N-5 nitrogen during anodic scan and vice versa for cathodic scan and (ii) one-electron conversion of pyridine to oxidized pyridine. Voltammograms are also slightly tilted, pointing to an increase

in resistance at higher sweep rates. Here again we see a sharp drop in the capacitance of about 45% upon increasing the sweep rate from 5 to 100 mV s<sup>-1</sup>. This drop can be correlated to the conductivity of the electrode material, which was prepared without Vulcan, and the absence of quaternary nitrogen which is known to improve conductivity of carbon-based materials.<sup>105,106</sup> C-PPy-NTs have favorable pore structure and active nitrogen groups on the surface, and a high capacitance is expected. This is only true for low scan rates as conductivity factor becomes determinant as the scan rate is increased, just as in the case of PPy-NT base sample.

It should be noted, however, that the capacitance fade in the case of C-PPy-NT (45%), which has intermediate conductivity among the investigated samples (Table 2), is between the capacitance fade of PPy-NT base (around 70% loss between 5 and 100 mV s<sup>-1</sup>) and PPy-NT salt sample (virtually no loss). Because nanotubular PPy samples and C-PPy-NTs are different in nature and capacitance fade agrees with the relative differences in their conductivity, we propose the following hypothesis. It is suspected that the absolute value of the material's gravimetric capacitance is predominantly related to the textural properties and the presence of surface functional groups, i.e., its surface chemistry, while capacitance fade is determined mainly by material conductivity. For the case of the materials studied here, this is supported by a linear relationship between capacitance fade (estimated from the potentiodynamic measurements at 5 and 100 mV s<sup>-1</sup>) and the conductivity (in log scale; measurements at 125 MPa were used) (Figure 10).

As physicochemical characterization of C-PPy-NT sample reveals a carbonaceous material rich in covalently bonded nitrogen and oxygen-surface functionalities, it is of special interest to investigate its catalytic activity toward ORR.

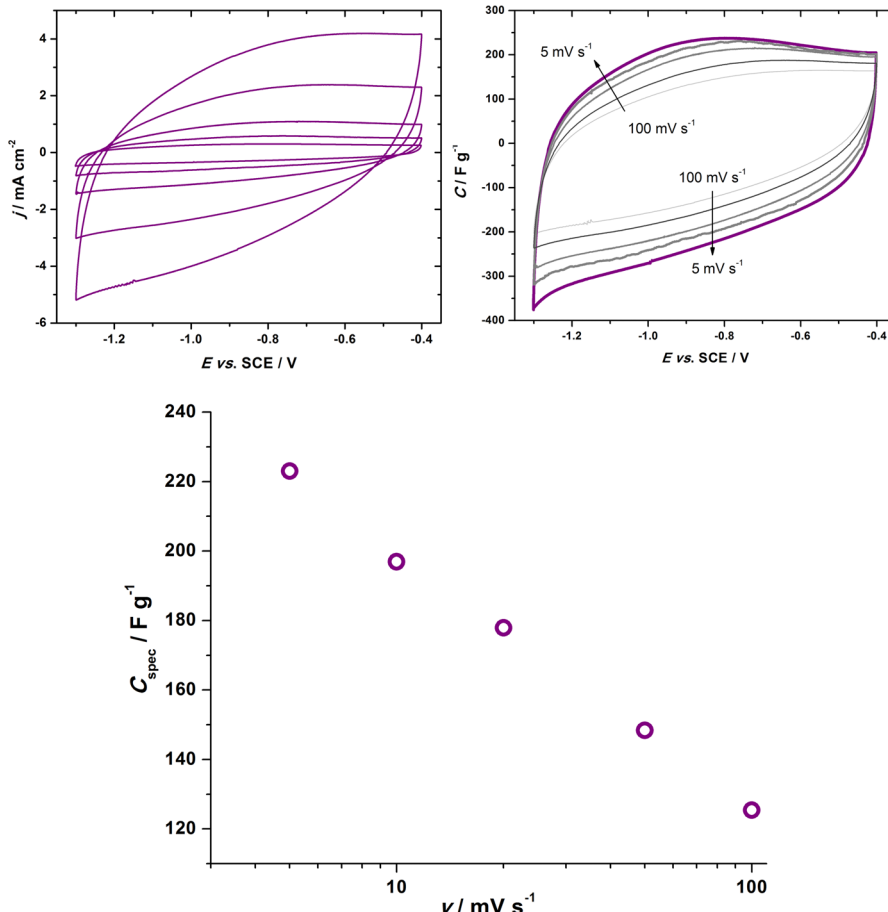


**Figure 9.** Cyclic voltammograms for C-PPy-NT-modified GC electrode at different potential sweep rates (top left panel) along with cyclic voltammograms normalized by potential sweep rate and C-PPy-NT loading (top right panel). In the bottom panel, the dependence of gravimetric capacitance of C-PPy-NT on the potential sweep rate is given.

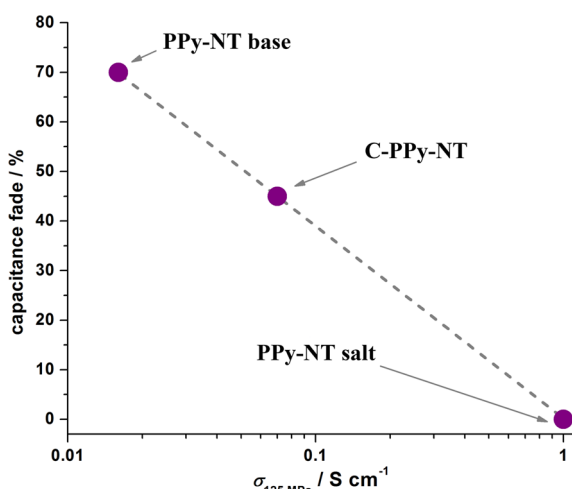


**Figure 10.** Dependence of the capacitance fade (estimated from the potentiodynamic measurements at 5 and 100 mV s<sup>-1</sup>) and a logarithm of the conductivity (measured at 125 MPa,  $\sigma_{125 \text{ MPa}}$ ).

Catalytic activity of C-PPy-NTs toward ORR, investigated using RDE voltammetry in oxygen-saturated 0.1 M aqueous potassium hydroxide solution, is rather high. Specifically, ORR onset potential was found to be as high as  $-0.1$  V versus SCE (Figure 11, top left panel). When compared to similar polymer-derived nitrogen-containing carbons in a series of PANI-based

carbonaceous materials investigated recently,<sup>16,51,52,76</sup> C-PPy-NTs investigated here stand side by side with some of the most active ones, including carbonized PANI 5-sulfosalicylate nanorods and nanotubes<sup>16</sup> and hydrothermally activated (at  $150$  °C) carbonized PANI hydrogen sulfate nanorods, nanotubes, and nanosheets.<sup>51</sup> However, the activity is somewhat lower than that of hydrothermally activated (at  $200$  °C) carbonized PANI hydrogen sulfate nanorods, nanotubes, and nanosheets.<sup>83</sup> The same holds when comparing mass activities (Figure 11, bottom left panel) of these materials.

ORR polarization curves were further subjected to the Koutecky–Levich (K-L) analysis<sup>107</sup> to determine the apparent number of electrons consumed per oxygen molecule,  $n(E)$ . The apparent number of electrons is determined from the slope of K-L lines defined by

$$\frac{1}{j(E)} = \frac{1}{j_k(E)} + \frac{1}{j_d(E)} = \frac{1}{j_k} - \frac{1}{0.62n(E)FD_{O_2}^{2/3}\nu^{-1/6}\omega^{1/2}c_{O_2}} \quad (1)$$

In eq 1,  $j(E)$ ,  $j_k(E)$ , and  $j_d(E)$  stand for measured current density, kinetic current density (free of mass-transfer limitations), and the limiting diffusion current density at the electrode potential  $E$ , respectively. In addition,  $\nu$  represents the kinematic viscosity of the solution ( $0.01 \text{ cm}^2 \text{ s}^{-1}$ <sup>108</sup>);  $D_{O_2}$  is the diffusion coefficient of  $O_2$  ( $1.9 \times 10^{-5} \text{ cm}^2 \text{ s}^{-1}$ <sup>109</sup>), and  $c_{O_2}$  is

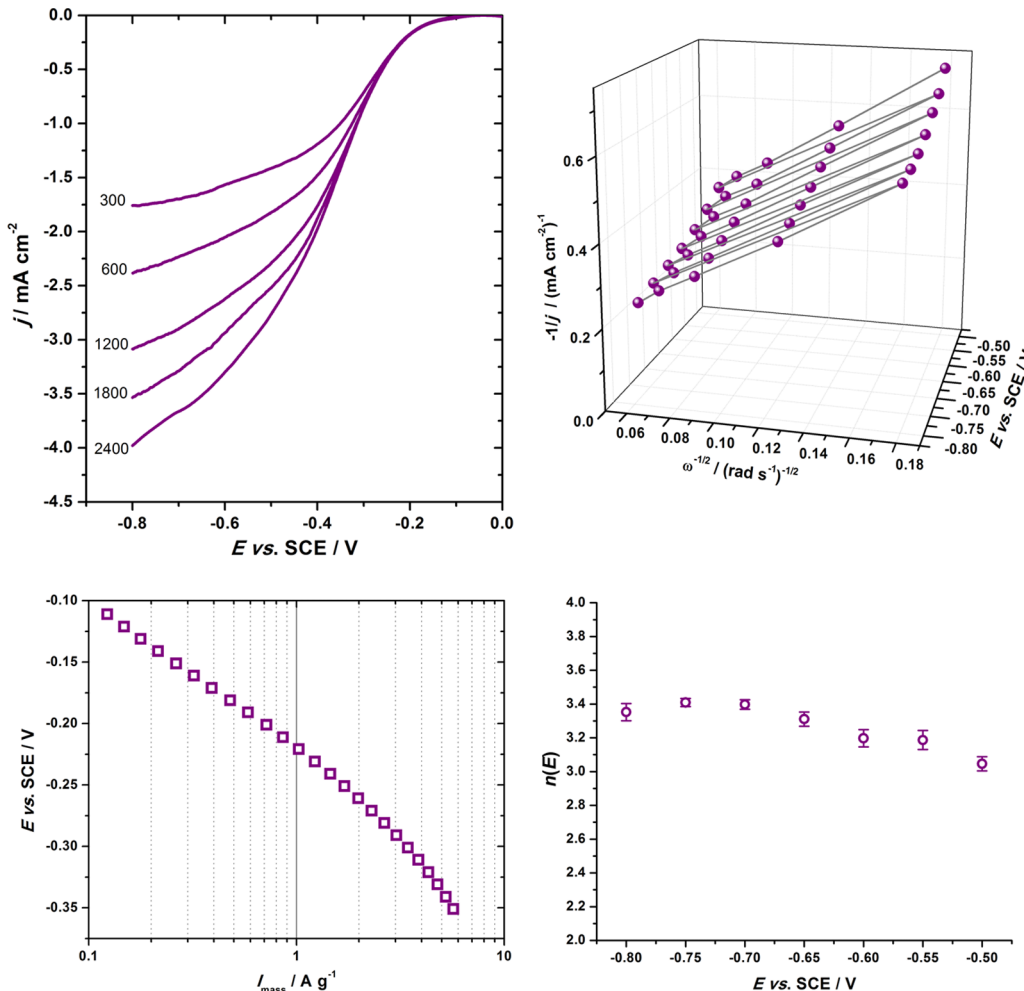


**Figure 11.** (Top left panel) Background-corrected ORR RDE polarization curves on C-PPy-NT-modified GC electrode at different electrode rotation rates (rpm); (bottom left panel) background- and mass-transfer-corrected ORR polarization curve evaluated per unit mass of C-PPy-NT to assess ORR mass-activity of the material ( $I_{\text{mass}}$ , presented in Tafel coordinates); (top right panel) Koutecky–Levich plots for ORR on C-PPy-NT-modified GC electrode at different electrode potentials; (bottom right panel) apparent number of electrons consumed per oxygen molecule,  $n(E)$ , as a function of the electrode potential, evaluated using Koutecky–Levich analysis. C-PPy-NT loading was  $250 \mu\text{g cm}^{-2}$ .

the concentration of dissolved  $\text{O}_2$  ( $1.2 \times 10^{-3} \text{ M}^{109}$ ). As defined, limiting diffusion current density depends on the physicochemical properties of the solution and electrode potential  $E$  in the same manner as  $n(E)$ . Obtained K-L plots (Figure 11, top right panel) at different  $E$  were straight lines with positive intercepts for the entire electrode potential window considered in this study ( $-0.8$  to  $-0.5$  V versus SCE), indicating that, for a given C-PPy-NT loading, ORR is under mixed control, while extracted  $n(E)$  values were between 3 (lower ORR overvoltage) and 3.4 (higher overvoltage) (Figure 11, bottom right). In this sense, too, C-PPy-NT compares well with the most active PANI-based nitrogen-containing carbon investigated recently,<sup>16</sup> but its performance is somewhat lower than that of hydrothermally activated (at  $200^\circ\text{C}$ ) carbonized PANI hydrogen sulfate nanorods, nanotubes, and nanosheets.<sup>83</sup> When compared to other carbonaceous materials reported in the literature, ORR performance of C-PPy-NT is comparable or better than ORR performance of some advanced carbonaceous materials. For example, a carbonized PPy/reduced graphene oxide composite developed by Ma et al.<sup>110</sup> provides similar ORR activity in terms of  $n(E)$ , but ORR onset potential was lower than that of C-PPy-NTs. It should be noted that in the present report C-PPy-NT has very low iron content (Table 3),

and its role on improvement of ORR kinetics is not very likely. This indicates that the carbonization of PPy could lead to nitrogen-containing carbonaceous materials with high ORR activity in alkaline media, with no need for formation of advanced composite materials, which reduces the price of such ORR catalysts. The performance of the investigated C-PPy-NT also supersedes that of N-doped carbon nanotubes investigated by Alexeyeva et al.<sup>111</sup> in terms of both ORR onset potential and  $n(E)$  (found to be below 3 in the potential window considered here for K-L analysis). These results are on par with those for codoped functional tubular polypyrrole reported recently by Liu et al.<sup>112</sup> when concerned with ORR onset potential. On the other hand, C-PPy-NTs reported here displayed somewhat lower values of apparent number of electrons consumed per oxygen molecule.

There is much debate about the role of specific nitrogen functionalities, but many authors agree that pyridinic and quaternary nitrogen affect the onset potential and limiting current density, respectively.<sup>113,114</sup> Exceptional ORR activity of C-PPy-NT can be rationalized on the basis of its physicochemical properties. It has a high surface nitrogen content (~12 atom %), all in pyridinic and pyrrolic/pyridone form as evidenced by XPS, which clearly has a positive effect on

electrocatalytic behavior toward ORR. Also, the material is highly mesoporous, which is, according to some researchers,<sup>15,16,115</sup> significant for easy reactant–product transport and disproportionation reaction which governs the mechanism of the ORR. C-PPy-NT fulfills several criteria for a good ORR catalyst: it has high surface nitrogen content, ORR active nitrogen moieties, balanced micro- and mesoporosity and relatively good conductivity which manifest in positive onset potential and high current densities and apparent number of electrons. It should also be noted that present C-PPy-NT is a highly disordered material, as seen through high D/G ratios in Raman spectra, and the presence of defects is known to contribute to high catalytic activity of carbonaceous materials.<sup>13</sup> The results provided here, and the ones earlier reported on similar materials,<sup>16,51,52,76,83</sup> could be a useful guide for development of new highly active noble-metal-free electrocatalysts for ORR with a promising applicability in alkaline fuel cells and metal–air batteries. However, a wider picture can be offered, too, as carbonaceous materials possess high versatility and a diverse range of possible applications;<sup>116</sup> in this special case, it appears that C-PPy-NT has promising applicability in the field of electrochemical capacitors, too.

## CONCLUSIONS

In the present work, nanotubular PPy was synthesized in salt and base forms. Upon carbonization of the salt form of PPy-NTs, a nanotubular conducting carbonaceous material was obtained, denoted as C-PPy-NT. TEM analysis revealed well-defined nanotubes with diameters between 70 and 300 nm and lengths of several micrometers. FTIR spectroscopy was used to assess characteristic functional groups, while Raman spectroscopy pointed to a high degree of structural disorder in the C-PPy-NT sample. Conductivity measurements indicated that the salt form of prepared PPy-NT is a good conductor, with conductivity in the order of siemens per centimeter determined for a compressed powder. On the other hand, conductivity of PPy-NT base was 2 orders of magnitude lower, while the C-PPy-NT had intermediate conductivity. For C-PPy-NT, surface nitrogen content was found to be around 12 atom %, and it was concluded that this sample has core–shell structure, the core and the shell being differentiated mutually by the degree of carbonization. Nitrogen physisorption has shown that non-carbonized samples have relatively low content of mesopores and low specific surface area of  $\approx 55 \text{ m}^2 \text{ g}^{-1}$ . Upon carbonization, the specific surface area increased more than 5 times and the fraction of mesopores significantly increased. Electrochemistry of noncarbonized samples was tested potentiodynamically in aqueous potassium chloride solution, and the experiments revealed specific capacitance of around  $120 \text{ F g}^{-1}$  at low potential sweep rates. PPy-NT salt retained an unchanged value of specific capacitance upon increasing potential sweep rate up to  $100 \text{ mV s}^{-1}$ , while the capacitance of PPy-NT base decreased by 70%. After carbonization, the specific capacitance measured in aqueous potassium hydroxide solution was doubled compared with that of noncarbonized PPy-NT, while the capacitance fade in the sweep rate range of  $5\text{--}100 \text{ mV s}^{-1}$  was found to be around 45%. It is proposed that the absolute value of specific capacitance is determined by specific surface area and surface functional groups, while capacitance fade is controlled by the conductivity of the electrode material. In this manner, a linear relationship between capacitance fade and a logarithm of the conductivity was found. C-PPy-NTs were also probed as an electrocatalyst for ORR in

alkaline media. High ORR activity was observed with onset potential at  $-0.1 \text{ V}$  versus SCE and apparent number of electrons consumed per oxygen molecule above 3. Appreciable ORR activity can be linked with a high fraction of mesopores and the presence of surface functional groups, especially pyridinic and pyrrolic nitrogen, and also a high degree of structural disorder, as revealed by Raman spectroscopy. Present results can be used as a guide for the preparation of advanced materials for electrochemical energy conversion and storage applications.

## AUTHOR INFORMATION

### Corresponding Author

\*E-mail: gordana@ffh.bg.ac.rs. Phone: +381 11 3336 633. Fax: +381 11 2187 133.

### Notes

The authors declare no competing financial interest.

## ACKNOWLEDGMENTS

This work was supported by the Serbian Ministry of Science and Technological Development (OI172043, III45014) and Czech Science Foundation (P205/12/0911, 13-00270S, 14-10279S). We thank Dr. Biljana Dođinović, University of Belgrade-ICTM, for performing ICP-OES measurements.

## REFERENCES

- (1) Kroto, H. W.; Heath, J. R.; O'Brien, S. C.; Curl, R. F.; Smalley, R. E.  $C_{60}$ : Buckminsterfullerene. *Nature (London, U.K.)* **1985**, *318*, 162–163.
- (2) Iijima, S. Helical Microtubules of Graphitic Carbon. *Nature (London, U.K.)* **1991**, *354*, 56–58.
- (3) Nieto-Márquez, A.; Romero, R.; Romero, A.; Valverde, J. L. Carbon Nanospheres: Synthesis, Physicochemical Properties and Applications. *J. Mater. Chem.* **2011**, *21*, 1664–1672.
- (4) De Jong, K. P.; Geus, J. W. Carbon Nanofibers: Catalytic Synthesis and Applications. *Catal. Rev.: Sci. Eng.* **2001**, *42*, 481–510.
- (5) Zhu, S.; Xu, G. Single-Walled Carbon Nanohorns and Their Applications. *Nanoscale* **2010**, *2*, 2538–2549.
- (6) Geim, A. K.; Novoselov, K. S. The Rise of Graphene. *Nat. Mater.* **2007**, *6*, 183–191.
- (7) Stephan, O.; Ajayan, P. M.; Colliex, C.; Redlich, P.; Lambert, J. M.; Bernier, P. M.; Lefin, P. Doping Graphitic and Carbon Nanotube Structures with Boron and Nitrogen. *Science* **1994**, *266*, 1683–1685.
- (8) Panchakarla, L. S.; Govindaraj, A.; Rao, C. N. R. Boron- and Nitrogen-Doped Carbon Nanotubes and Graphene. *Inorg. Chim. Acta* **2010**, *363*, 4163–4174.
- (9) Yang, Z.; Nie, H.; Chen, X.; Chen, X.; Huang, S. Recent Progress in Doped Carbon Nanomaterials as Effective Cathode Catalysts for Fuel Cell Oxygen Reduction Reaction. *J. Power Sources* **2013**, *236*, 238–249.
- (10) Maiti, U. N.; Lee, W. J.; Lee, J. M.; Oh, Y.; Kim, J. Y.; Kim, J. E.; Shim, J.; Han, T. H.; Kim, S. O. Chemically Modified/Doped Carbon Nanotubes & Graphene for Optimized Nanostructures & Nano-devices. *Adv. Mater. (Weinheim, Ger.)* **2014**, *26*, 40–67.
- (11) Ewels, C. P.; Glerup, M. Nitrogen Doping in Carbon Nanotubes. *J. Nanosci. Nanotechnology* **2005**, *5*, 1345–1363.
- (12) Ayala, P.; Arenal, R.; Rummeli, M.; Rubio, A.; Pichler, T. The Doping of Carbon Nanotubes with Nitrogen and Their Potential Applications. *Carbon* **2010**, *48*, 575–586.
- (13) Wong, W. Y.; Daud, W. R. W.; Mohamad, A. B.; Kadhum, A. A. H.; Majlan, E. H.; Loh, K. S. Nitrogen-Containing Carbon Nanotubes as Cathodic Catalysts for Proton Exchange Membrane Fuel Cells. *Diamond Relat. Mater.* **2012**, *22*, 12–22.
- (14) Li, Y.; Wang, J.; Li, X.; Liu, J.; Geng, D.; Yang, J.; Li, R.; Sun, X. Nitrogen-Doped Carbon Nanotubes as Cathode for Lithium-Air Batteries. *Electrochim. Commun.* **2011**, *13*, 668–672.

- (15) Gavrilov, N.; Pašti, I. A.; Vujković, M.; Travas-Sejdic, J.; Ćirić-Marjanović, G.; Mentus, S. V. High-Performance Charge Storage by N-Containing Nanostructured Carbon Derived from Polyaniline. *Carbon* **2012**, *50*, 3915–3927.
- (16) Gavrilov, N.; Pašti, I. A.; Mitić, M.; Travas-Sejdić, J.; Ćirić-Marjanović, G.; Mentus, S. V. Electrocatalysis of Oxygen Reduction Reaction on Polyaniline-Derived Nitrogen-Doped Carbon Nanoparticle Surfaces in Alkaline Media. *J. Power Sources* **2012**, *220*, 306–316.
- (17) Chen, Y. Z.; Zhu, H. Y.; Liu, Y. N. Preparation of Activated Rectangular Polyaniline-Based Carbon Tubes and Their Application in Hydrogen Adsorption. *Int. J. Hydrogen Energy* **2011**, *36*, 11738–11745.
- (18) Rebollo-Plata, B.; Munoz-Sandoval, E.; Lopez-Urias, F.; Hernandez-Cortina, E. L.; Terrones, H.; Terrones, M. Efficient Vapor Sensors Using Foils of Dispersed Nitrogen-Doped and Pure Carbon Multiwalled Nanotubes. *J. Nanosci. Nanotechnol.* **2010**, *10*, 3965–3972.
- (19) Xu, X.; Jiang, S.; Hu, Z.; Liu, S. Nitrogen-Doped Carbon Nanotubes: High Electrocatalytic Activity Toward the Oxidation of Hydrogen Peroxide and Its Application for Biosensing. *ACS Nano* **2010**, *4*, 4292–4298.
- (20) Van Dommelle, S.; De Jong, K. P.; Bitter, J. H. Activity of Nitrogen Containing Carbon Nanotubes in Base Catalyzed Knovenagel Condensation. *Top. Catal.* **2009**, *52*, 1575–1583.
- (21) Perez-Aguilar, N. V.; Munoz-Sandoval, E.; Diaz-Flores, P. E.; Rangel-Mendez, J. R. Adsorption of Cadmium and Lead onto Oxidized Nitrogen-Doped Multiwall Carbon Nanotubes in Aqueous Solution: Equilibrium and Kinetics. *J. Nanopart. Res.* **2010**, *12*, 467–480.
- (22) Laiho, P.; Susi, T.; Askela, A.; Nasibulin, A. G.; Kauppinen, E. I. Optoelectronic Performance of Nitrogen-Doped Single-Walled Carbon Nanotube Films. *J. Nanoelectron. Optoelectron.* **2012**, *7*, 68–72.
- (23) Goran, J. M.; Mantilla, S. M.; Stevenson, K. J. Influence of Surface Adsorption on the Interfacial Electron Transfer of Flavin Adenine Dinucleotide and Glucose Oxidase at Carbon Nanotube and Nitrogen-Doped Carbon Nanotube Electrodes. *Anal. Chem.* **2013**, *85*, 1571–1581.
- (24) Alidori, S.; Asqiriba, K.; Londero, P.; Bergkvist, M.; Leona, M.; Scheinberg, D. A.; McDevitt, M. R. Deploying RNA and DNA with Functionalized Carbon Nanotubes. *J. Phys. Chem. C* **2013**, *117*, 5982–5992.
- (25) Santana, C.; Garcia, A.; Perez, J.; Hoyos, L.; Martinez, V.; Bustamante, J. Nitrogen, potassium and aluminum doped carbon nanotubes for atheroma-lipoproteins interaction on atherosclerosis treatment. Proceedings of the 2013 Pan American Health Care Exchanges (PAHCE), Medellin, Colombia, April 29–May 4, 2013; DOI: 10.1109/PAHCE.2013.6568282.
- (26) Chen, Z.; Dai, X. J.; Magniez, K.; Lamb, P. R.; de Celis Leal, D. R.; Fox, B. L.; Wang, X. Improving the Mechanical Properties of Epoxy Using Multiwalled Carbon Nanotubes Functionalized by a Novel Plasma Treatment. *Composites, Part A* **2013**, *45*, 145–152.
- (27) Yin, J.; Xia, X.; Xiang, L.; Zhao, X. Conductivity and Polarization of Carbonaceous Nanotubes Derived from Polyaniline Nanotubes and Their Electrorheology When Dispersed in Silicone Oil. *Carbon* **2010**, *48*, 2958–2967.
- (28) Wu, C.; Guo, Q.; Yin, P.; Li, T.; Yang, Q.; Xie, Y. Synthesis of Nitrogen-Doped Carbon Nanostructures by the Reactions of Small Molecule Carbon Halides with Sodium Azide. *J. Phys. Chem. B* **2005**, *109*, 2597–2604.
- (29) Wu, X.; Tao, Y.; Mao, C.; Wen, L.; Zhu, J. Synthesis of Nitrogen-Doped Horn-Shaped Carbon Nanotubes by Reduction of Pentachloropyridine with Metallic Sodium. *Carbon* **2007**, *45*, 2253–2259.
- (30) Droppa, R., Jr.; Hammer, P.; Carvalho, A. C. M.; Dos Santos, M. C.; Alvarez, F. Incorporation of Nitrogen in Carbon Nanotubes (Part 2). *J. Non-Cryst. Solids* **2002**, *299*–*302*, 874–879.
- (31) Lin, H.; Lagoute, J.; Chacon, C.; Arenal, R.; Stephan, O.; Repain, V.; Girard, Y.; Enouz, S.; Bresson, L.; Rousset, S.; Loiseau, A. Combined STM/STS, TEM/EELS Investigation of CN<sub>x</sub>-SWNTs. *Phys. Status Solidi B* **2008**, *245*, 1986–1989.
- (32) Cao, L. M.; Zhang, X. Y.; Gao, C. X.; Wang, W. K.; Zhang, Z. L.; Zhang, Z. High-Concentration Nitrogen-Doped Carbon Nanotube Arrays. *Nanotechnology* **2003**, *14*, 931–934.
- (33) Blank, V. D.; Polyakov, E. V.; Batov, D. V.; Kulnitskiy, B. A.; Bangert, U.; Gutierrez-Sosa, A.; Harvey, A. J.; Seepujak, A. Formation of N-Containing C-Nanotubes and Nanofibres by Carbon Resistive Heating under High Nitrogen Pressure. *Diamond Relat. Mater.* **2003**, *12*, 864–869.
- (34) Badzian, A.; Badzian, T.; Breval, E.; Piotrowski, A. Nanostructured, Nitrogen-Doped Carbon Materials for Hydrogen Storage. *Thin Solid Films* **2001**, *398*–*399*, 170–174.
- (35) Bulusheva, L. G.; Okotrub, A. V.; Kudashov, A. G.; Shubin, Y. V.; Shlyakhova, E. V.; Yudanov, N. F.; Pazhetnov, E. M.; Boronin, A. I.; Vyalikh, D. V. Effect of Fe/Ni Catalyst Composition on Nitrogen Doping and Field Emission Properties of Carbon Nanotubes. *Carbon* **2008**, *46*, 864–869.
- (36) Jian, G.; Zhao, Y.; Wu, Q.; Yang, L.; Wang, X.; Hu, Z. Structural and Compositional Regulation of Nitrogen-Doped Carbon Nanotubes with Nitrogen-Containing Aromatic Precursors. *J. Phys. Chem. C* **2013**, *117*, 7811–7817.
- (37) Shan, C.; Zhao, W.; Lu, X. L.; O'Brien, D. J.; Li, Y.; Cao, Z.; Elias, A. L.; Cruz-Silva, R.; Terrones, M.; Wei, B.; Suhr, J. Three-Dimensional Nitrogen-Doped Multiwall Carbon Nanotube Sponges with Tunable Properties. *Nano Lett.* **2013**, *13*, 5514–5520.
- (38) Ning, G.; Xu, C.; Zhu, X.; Zhang, R.; Qian, W.; Wei, F.; Fan, Z.; Gao, J. MgO-Catalyzed Growth of N-Doped Wrinkled Carbon Nanotubes. *Carbon* **2013**, *56*, 38–44.
- (39) Allen, B. L.; Keddie, M. B.; Star, A. Controlling the volumetric parameters of nitrogen-doped carbon nanotube cups. *Nanoscale* **2010**, *2*, 1105–1108.
- (40) Chen, C.; Liang, B.; Lu, D.; Ogino, A.; Wang, X.; Nagatsu, M. Amino Group Introduction onto Multiwall Carbon Nanotubes by NH<sub>3</sub>/Ar Plasma Treatment. *Carbon* **2010**, *48*, 939–948.
- (41) Xu, F.; Minniti, M.; Barone, P.; Sindona, A.; Bonanno, A.; Oliva, A. Nitrogen Doping of Single Walled Carbon Nanotubes by Low Energy N<sub>2</sub><sup>+</sup> Ion Implantation. *Carbon* **2008**, *46*, 1489–1496.
- (42) Wang, P. C.; Liao, Y. C.; Lai, Y. L.; Lin, Y. C.; Su, C. Y.; Tsai, C. H.; Hsu, Y. J. Thermally Induced Variation in Redox Chemical Bonding Structures of Single-Walled Carbon Nanotubes Exposed to Hydrazine Vapor. *Carbon* **2012**, *50*, 1650–1658.
- (43) Viikkilä, M.; Kruusenberg, I.; Joost, U.; Shulga, E.; Tammeveski, K. Electrocatalysis of Oxygen Reduction on Nitrogen-Containing Multi-walled Carbon Nanotube Modified Glassy Carbon Electrodes. *Electrochim. Acta* **2013**, *87*, 709–716.
- (44) He, C.; Shen, P. K. Synthesis of the Nitrogen-Doped Carbon Nanotube (NCNT) Bouquets and Their Electrochemical Properties. *Electrochim. Commun.* **2013**, *35*, 80–83.
- (45) Maiyalagan, T. Synthesis and Electro-catalytic Activity of Methanol Oxidation on Nitrogen Containing Carbon Nanotubes Supported Pt Electrodes. *Appl. Catal., B* **2008**, *80*, 286–295.
- (46) Ćirić-Marjanović, G.; Pašti, I.; Gavrilov, N.; Janošević, A.; Mentus, S. Carbonized Polyaniline and Pyrrole: Towards Advanced Nitrogen-Containing Carbon Materials. *Chem. Pap.* **2013**, *67*, 781–813.
- (47) Ćirić-Marjanović, G. Recent Advances in Polyaniline Research: Polymerization Mechanisms, Structural Aspects, Properties and Applications. *Synth. Met.* **2013**, *177*, 1–47.
- (48) Mentus, S.; Ćirić-Marjanović, G.; Trchová, M.; Stejskal, J. Conducting Carbonized Polyaniline Nanotubes. *Nanotechnology* **2009**, *20*, 245601.
- (49) Trchová, M.; Konyushenko, E. N.; Stejskal, J.; Kovařová, J.; Ćirić-Marjanović, G. The Conversion of Polyaniline Nanotubes to Nitrogen-Containing Carbon Nanotubes and Their Comparison with Multiwalled Carbon Nanotubes. *Polym. Degrad. Stab.* **2009**, *94*, 929–938.
- (50) Gavrilov, N.; Dašić-Tomić, M.; Pašti, I.; Ćirić-Marjanović, G.; Mentus, S. Carbonized Polyaniline Nanotubes/Nanosheets-Supported Pt Nanoparticles: Synthesis, Characterization and Electrocatalysis. *Mater. Lett.* **2011**, *65*, 962–965.

- (51) Gavrilov, N.; Vujković, M.; Pašti, I. A.; Čirić-Marjanović, G.; Mentus, S. V. Enhancement of Electrocatalytic Properties of Carbonized Polyaniline Nanoparticles Upon a Hydrothermal Treatment in Alkaline Medium. *Electrochim. Acta* **2011**, *56*, 9197–9202.
- (52) Janošević, A.; Pašti, I.; Gavrilov, N.; Mentus, S.; Čirić-Marjanović, G.; Krstić, J.; Stejskal, J. Micro/Mesoporous Conducting Carbonized Polyaniline 5-Sulfosalicylate Nanorods/Nanotubes: Synthesis, Characterization and Electrocatalysis. *Synth. Met.* **2011**, *161*, 2179–2184.
- (53) Jang, J.; Oh, J. H. A Facile Synthesis of Polypyrrole Nanotubes Using a Template Mediated Vapor Deposition Polymerization and the Conversion to Carbon Nanotubes. *Chem. Commun. (Cambridge, U.K.)* **2004**, *7*, 882–883.
- (54) Zhang, X.; Manohar, S. K. Microwave Synthesis of Nanocarbons from Conducting Polymers. *Chem. Commun. (Cambridge, U.K.)* **2006**, *31*, 2477–2479.
- (55) Dong, H.; Jones, W. E., Jr. Preparation of Submicron Polypyrrole/Poly(methyl methacrylate) Coaxial Fibers and Conversion to Polypyrrole Tubes and Carbon Tubes. *Langmuir* **2006**, *22*, 11384–11387.
- (56) Shang, S.; Yang, X.; Tao, X. M. Easy Synthesis of Carbon Nanotubes with Polypyrrole Nanotubes as the Carbon Precursor. *Polymer* **2009**, *50*, 2815–2818.
- (57) Bae, J.; Jang, J. Fabrication of Carbon Nanotubes from Conducting Polymer Precursor as Field Emitter. *J. Ind. Eng. Chem.* **2012**, *18*, 1921–1924.
- (58) Xu, G.; Ding, B.; Nie, P.; Shen, L.; Wang, J.; Zhang, X. Porous Nitrogen-Doped Carbon Nanotubes Derived from Tubular Polypyrrole for Energy-Storage Applications. *Chem.—Eur. J.* **2013**, *19*, 12306–12312.
- (59) Liu, Q.; Pu, Z.; Tang, C.; Asiri, A. M.; Qusti, A. H.; Al-Youbi, A. O.; Sun, X. N-Doped Carbon Nanotubes from Functional Tubular Polypyrrole: A Highly Efficient Electrocatalyst for Oxygen Reduction Reaction. *Electrochim. Commun.* **2013**, *36*, 57–61.
- (60) Wu, M.; Chena, J.; Wangc, C.; Wangf, F.; Yia, B. Non-graphitic PPy-Based Carbon Nanotubes Anode Materials for Lithium-ion Batteries. *Electrochim. Acta* **2013**, *105*, 462–467.
- (61) Guo, C.; Li, N.; Ji, L.; Li, Y.; Yang, X.; Lu, Y.; Tu, Y. N- and O-Doped Carbonaceous Nanotubes from Polypyrrole for Potential Application in High-Performance Capacitance. *J. Power Sources* **2014**, *247*, 660–666.
- (62) Yang, X. M.; Zhu, Z. X.; Dai, T. Y.; Lu, Y. Facile Fabrication of Functional Polypyrrole Nanotubes via a Reactive Self-degraded Template. *Macromol. Rapid Commun.* **2005**, *26*, 1736–1740.
- (63) Skodova, J.; Kopecky, D.; Vrnata, M.; Varga, M.; Prokes, J.; Cieslar, M.; Bober, P.; Stejskal, J. Polypyrrole-Silver Composites Prepared by the Reduction of Silver Ions with Polypyrrole Nanotubes. *Polym. Chem.* **2013**, *4*, 3610–3616.
- (64) Kopecka, J.; Kopecky, D.; Vrnata, M.; Fitl, P.; Stejskal, J.; Trchová, M.; Bober, P.; Moravkova, Z.; Prokes, J.; Sapurina, I. Polypyrrole Nanotubes: Mechanism of Formation. *RSC Adv.* **2014**, *4*, 1551–1558.
- (65) Wang, Z.; Qie, L.; Yuan, L.; Zhang, W.; Hu, X.; Huang, Y. Functionalized N-Doped Interconnected Carbon Nanofibers as an Anode Material for Sodium-ion Storage with Excellent Performance. *Carbon* **2013**, *55*, 328–334.
- (66) Blinova, N. V.; Stejskal, J.; Trchová, M.; Prokeš, J.; Omastová, M. Polyaniline and Polypyrrole: A Comparative Study of the Preparation. *Eur. Polym. J.* **2007**, *43*, 2331–2341.
- (67) Omastová, M.; Trchová, M.; Kovářová, J.; Stejskal, J. Synthesis and Structural Study of Polypyrroles Prepared in the Presence of Surfactants. *Synth. Met.* **2003**, *138*, 447–455.
- (68) Furukawa, Y.; Tazawa, S.; Fujii, Y.; Harada, I. Raman Spectra of Polypyrrole and its 2,5-<sup>13</sup>C-Substituted and C-Deuterated Analogues in Doped and Undoped States. *Synth. Met.* **1988**, *24*, 329–341.
- (69) Zhong, C. J.; Tian, Z. Q.; Tian, Z. W. In Situ ESR and Raman Spectroscopic Studies of the Electrochemical Process of Conducting Polypyrrole Films. *J. Phys. Chem.* **1990**, *94*, 2171–2175.
- (70) Jenden, C. M.; Davidson, R. G.; Turner, T. G. A Fourier Transform-Raman Spectroscopic Study of Electrically Conducting Polypyrrole Films. *Polymer* **1993**, *34*, 1649–1652.
- (71) Kostić, R.; Raković, D.; Stepanyan, S. A.; Davidova, I. E.; Gribov, L. A. Vibrational Spectroscopy of Polypyrrole, Theoretical-Study. *J. Chem. Phys.* **1995**, *102*, 3104–3109.
- (72) Gupta, S. Hydrogen Bubble-Assisted Syntheses of Polypyrrole Micro/Nanostructures Using Electrochemistry: Structural and Physical Property Characterization. *J. Raman Spectrosc.* **2008**, *39*, 1343–1355.
- (73) Dresselhaus, M. S.; Jorio, A.; Hofmann, M.; Dresselhaus, G.; Saito, R. Perspectives on Carbon Nanotubes and Graphene Raman Spectroscopy. *Nano Lett.* **2010**, *10*, 751–758.
- (74) van Dommele, S.; de Jong, K. P.; Bitter, J. H. Nitrogen-Containing Carbon Nanotubes as Solid Base Catalysts. *Chem. Commun. (Cambridge, U.K.)* **2006**, *4859*–4861.
- (75) Rozlívková, Z.; Trchová, M.; Exnerová, M.; Stejskal, J. The Carbonization of Granular Polyaniline to Produce Nitrogen-Containing Carbon. *Synth. Met.* **2011**, *161*, 1122–1129.
- (76) Janošević, A.; Pašti, I.; Gavrilov, N.; Mentus, S.; Krstić, J.; Mitić, M.; Travas-Sejdic, J.; Čirić-Marjanović, G. Microporous Conducting Carbonized Polyaniline Nanorods: Synthesis, Characterization and Electrocatalytic Properties. *Microporous Mesoporous Mater.* **2012**, *152*, 50–57.
- (77) Maldonado, S.; Stevenson, K. J. Direct Preparation of Carbon Nanofiber Electrodes via Pyrolysis of Iron(II) Phthalocyanine: Electrocatalytic Aspects for Oxygen Reduction. *J. Phys. Chem. B* **2004**, *108*, 11375–11383.
- (78) Chun, K.-Y.; Lee, H. S.; Lee, C. J. Nitrogen Doping Effects on the Structure Behavior and the Field Emission Performance of Double-Walled Carbon Nanotubes. *Carbon* **2009**, *47*, 169–177.
- (79) Zhang, L.; Xia, Z. Mechanisms of Oxygen Reduction Reaction on Nitrogen-Doped Graphene for Fuel Cells. *J. Phys. Chem. C* **2011**, *115*, 11170–11176.
- (80) Kundu, S.; Nagaiah, T. C.; Xia, W.; Wang, Y.; Dommele, S. V.; Bitter, J. H.; Santa, M.; Grundmeier, G.; Bron, M.; Schuhmann, W.; Muhler, M. Electrocatalytic Activity and Stability of Nitrogen-Containing Carbon Nanotubes in the Oxygen Reduction Reaction. *J. Phys. Chem. C* **2009**, *113*, 14302–14310.
- (81) Niwa, H.; Kobayashi, M.; Horiba, K.; Harada, Y.; Oshima, M.; Terakura, K.; Ikeda, T.; Koshigoe, Y.; Ozaki, J.-i.; Miyata, S.; Ueda, S.; Yamashita, Y.; Yoshikawa, H.; Kobayashi, K. X-ray Photoemission Spectroscopy Analysis of N-Containing Carbon-Based Cathode Catalysts for Polymer Electrolyte Fuel Cells. *J. Power Sources* **2011**, *196*, 1006–1011.
- (82) Liu, G.; Li, X.; Ganesan, P.; Popov, B. N. Studies of Oxygen Reduction Reaction Active Sites and Stability of Nitrogen-Modified Carbon Composite Catalysts for PEM Fuel Cells. *Electrochim. Acta* **2010**, *55*, 2853–2858.
- (83) Vujković, M.; Gavrilov, N.; Pašti, I.; Krstić, J.; Travas-Sejdic, J.; Čirić-Marjanović, G.; Mentus, S. Superior Capacitive and Electrocatalytic Properties of Carbonized Nanostructured Polyaniline upon a Low-Temperature Hydrothermal Treatment. *Carbon* **2013**, *64*, 472–486.
- (84) Nasef, M. M.; Saidi, H.; Nor, H. M.; Yarmo, M. A. XPS Studies of Radiation Grafted PTFE-g-polystyrene Sulfonic Acid Membranes. *J. Appl. Polym. Sci.* **2000**, *76*, 336–349.
- (85) Morozan, A.; Jégou, P.; Campidelli, S.; Palacin, S.; Jouselme, B. Relationship Between Polypyrrole Morphology and Electrochemical Activity Towards Oxygen Reduction Reaction. *Chem. Commun. (Cambridge, U.K.)* **2012**, *48*, 4627–4629.
- (86) Maldonado, S.; Stevenson, K. J. Influence of Nitrogen Doping on Oxygen Reduction Electrocatalysis at Carbon Nanofiber Electrodes. *J. Phys. Chem. B* **2005**, *109*, 4707–4716.
- (87) Kelemen, S. R.; Gorbaty, M. L.; Kwiatek, P. J. Quantification of Nitrogen Forms in Argonne Premium Coals. *Energy Fuels* **1994**, *8*, 896–906.
- (88) Rouquerol, F.; Rouquerol, J.; Sing, K. *Adsorption by Powders and Porous Solids*; Academic Press: Waltham, MA, 1999.

- (89) Gregg, S. J.; Sing, K. S. W. *Adsorption, Surface Area and Porosity*; Academic Press: London, 1982.
- (90) Dollimore, D.; Heal, G. R. An Improved Method for the Calculation of Pore Size Distribution from Adsorption Data. *J. Appl. Chem.* **1964**, *14*, 109–114.
- (91) Horvath, G.; Kawazoe, K. Method for the Calculation of Effective Pore Size Distribution in Molecular Sieve Carbon. *J. Chem. Eng. Jpn.* **1983**, *16*, 470–475.
- (92) Dubinin, M. M. In *Progress in Surface and Membrane Science*; Cadenhead, D. A., Ed.; Academic Press: New York, 1975; p 1.
- (93) Shi, C.; Zhitomirsky, I. Electrodeposition and Capacitive Behavior of Films for Electrodes of Electrochemical Supercapacitors. *Nanoscale Res. Lett.* **2010**, *5*, 518–523.
- (94) Fan, L.-Z.; Maier, J. High-Performance Polypyrrole Electrode Materials for Redox Supercapacitors. *Electrochim. Commun.* **2006**, *8*, 937–940.
- (95) Ramya, R.; Sivasubramanian, R.; Sangaranarayanan, M. V. Conducting Polymers-Based Electrochemical Supercapacitors—Progress and Prospects. *Electrochim. Acta* **2013**, *101*, 109–129.
- (96) Huang, J.; Wang, K.; Wei, Z. Conducting Polymer Nanowire Arrays with Enhanced Electrochemical Performance. *J. Mater. Chem.* **2010**, *20*, 1117–1121.
- (97) Xu, B.; Zheng, D.; Jia, M.; Cao, G.; Yang, Y. Nitrogen-Doped Porous Carbon Simply Prepared by Pyrolyzing a Nitrogen-Containing Organic Salt for Supercapacitors. *Electrochim. Acta* **2013**, *98*, 176–182.
- (98) Yang, X.; Wu, D.; Chen, X.; Fu, R. Nitrogen-Enriched Nanocarbons with a 3-D Continuous Mesopore Structure from Polyacrylonitrile for Supercapacitor Application. *J. Phys. Chem. C* **2010**, *114*, 8581–8586.
- (99) Pandolfo, A. G.; Hollenkamp, A. F. Carbon Properties and Their Role in Supercapacitors. *J. Power Sources* **2006**, *157*, 11–27.
- (100) Xu, B.; Wu, F.; Su, Y.; Cao, G.; Chen, S.; Zhou, Z.; Yang, Y. Competitive Effect of KOH Activation on the Electrochemical Performances of Carbon Nanotubes for EDLC: Balance Between Porosity and Conductivity. *Electrochim. Acta* **2008**, *53*, 7730–7735.
- (101) Sánchez-González, J.; Stoeckli, F.; Centeno, T. A. The Role of the Electric Conductivity of Carbons in the Electrochemical Capacitor Performance. *J. Electroanal. Chem.* **2011**, *657*, 176–180.
- (102) Zhou, Z.; Zhang, Z.; Peng, H.; Qin, Y.; Li, G.; Chen, K. Nitrogen- and Oxygen-Containing Activated Carbon Nanotubes with Improved Capacitive Properties. *RSC Adv.* **2014**, *4*, 5524–5530.
- (103) Su, F.; Poh, C. K.; Chen, J. S.; Xu, G.; Wang, D.; Li, Q.; Lin, J.; Lou, X. W. Nitrogen-Containing Microporous Carbon Nanospheres with Improved Capacitive Properties. *Energy Environ. Sci.* **2011**, *4*, 717–724.
- (104) Wang, D.-W.; Li, F.; Yin, L.-C.; Lu, X.; Chen, Z.-G.; Gentle, I. R.; Lu, G. Q.; Cheng, H.-M. Nitrogen-Doped Carbon Monolith for Alkaline Supercapacitors and Understanding Nitrogen-Induced Redox Transitions. *Chem.—Eur. J.* **2012**, *18*, 5345–5351.
- (105) Seredych, M.; Hulicova-Jurcakova, D.; Lu, G. Q.; Bandosz, T. J. Surface Functional Groups of Carbons and the Effects of Their Chemical Character, Density and Accessibility to Ions on Electrochemical Performance. *Carbon* **2008**, *46*, 1475–1488.
- (106) Jalkanen, T.; Mäkilä, E.; Suzuki, Y. I.; Urata, T.; Fukami, K.; Sakka, T.; Salonen, J.; Ogata, Y. H. Studies on Chemical Modification of Porous Silicon-Based Graded-Index Optical Microcavities for Improved Stability under Alkaline Conditions. *Adv. Funct. Mater.* **2012**, *22*, 3890–3898.
- (107) Bard, A. J.; Faulkner, L. R. *Electrochemical Methods: Fundamentals and Applications*, 2nd ed.; Wiley: New York, 2001.
- (108) CRC *Handbook of Chemistry and Physics*, 82nd ed.; Lide, D. R., Ed.; CRC Press: Boca Raton, FL, 2001.
- (109) Davis, R. E.; Horvath, G. L.; Tobias, C. W. The Solubility and Diffusion Coefficient of Oxygen in Potassium Hydroxide Solutions. *Electrochim. Acta* **1967**, *12*, 287–298.
- (110) Ma, Y.; Zhang, L.; Li, J.; Ni, H.; Li, M.; Zhang, J.; Feng, X.; Fan, Q.; Hu, Z.; Huang, W. Carbon-Nitrogen/Graphene Composite as Metal-Free Electrocatalyst for the Oxygen Reduction Reaction. *Chin. Sci. Bull.* **2011**, *56*, 3583–3589.
- (111) Alexeyeva, N.; Shulga, E.; Kisand, V.; Kink, I.; Tammeveski, K. Electroreduction of Oxygen on Nitrogen-Doped Carbon Nanotube Modified Glassy Carbon Electrodes in Acid and Alkaline Solutions. *J. Electroanal. Chem.* **2010**, *648*, 169–175.
- (112) Liu, Q.; Pu, Z.; Tang, C.; Asiri, A. M.; Qusti, A. H.; Al-Youbi, A. O.; Sun, X. N-Doped Carbon Nanotubes from Functional Tubular Polypyrrole: A Highly Efficient Electrocatalyst for Oxygen Reduction Reaction. *Electrochim. Commun.* **2013**, *36*, 57–61.
- (113) Liu, R.; Wu, D.; Feng, X.; Müllen, K. Nitrogen-Doped Ordered Mesoporous Graphitic Arrays with High Electrocatalytic Activity for Oxygen Reduction. *Angew. Chem., Int. Ed.* **2010**, *49*, 2565–2569.
- (114) Ai, K.; Liu, Y.; Ruan, C.; Lu, L.; Lu, G. Sp<sup>2</sup> C-Dominant N-Doped Carbon Sub-micrometer Spheres with a Tunable Size: A Versatile Platform for Highly Efficient Oxygen-Reduction Catalysts. *Adv. Mater. (Weinheim, Ger.)* **2013**, *25*, 998–1003.
- (115) Rufford, T. E.; Hulicova-Jurcakova, D.; Zhu, Z.; Lu, G. Q. Empirical Analysis of the Contributions of Mesopores and Micropores to the Double-Layer Capacitance of Carbons. *J. Phys. Chem. C* **2009**, *113*, 19335–19343.
- (116) Momčilović, M.; Stojmenović, M.; Gavrilov, N.; Pašti, I.; Mentus, S.; Babić, B. Complex Electrochemical Investigation of Ordered Mesoporous Carbon Synthesized by Soft-Templating Method: Charge Storage and Electrocatalytical or Pt-Electrocatalyst Supporting Behavior. *Electrochim. Acta* **2014**, *125*, 606–614.